

NUWC-NPT Technical Report 10,820
6 October 1997

Beamformed Nearfield Imaging of a Simulated Coronary Artery Containing a Stenosis

**Andrew J. Hull
Norman L. Owsley
Submarine Sonar Department**



19971117 076

**Naval Undersea Warfare Center Division
Newport, Rhode Island**

Approved for public release; distribution is unlimited.

DEC 01 1997 11 17 076

PREFACE

Andrew J. Hull (Code 2141) was funded under the NUWC Division Newport Independent Research (IR) Program, Job Order No. B100047, "Noninvasive Passive Detection, Localization, and Characterization of Early Stage Arterial Disease." The IR program is funded by the Office of Naval Research; the NUWC Division Newport Program Manager is S. C. Dickinson (Code 102). Norman L. Owsley (Code 2123) was funded under Job Order No. N680217 through a Cooperative Research and Development Agreement (CRADA) sponsored by the Division's Technology Transfer Program, Manager Margaret M. McNamara (Code 105). The CRADA, entitled "Noninvasive Identification of Signals Generated During the Human Cardiac Cycle," was funded by MedAcoustics Corporation. Equipment support was provided through the Division's Bid and Proposal Program under Job Order No. A90602, "Noninvasive Detection and Localization of Signals in a Three-Dimensional Elastic Medium with Application to Artery Disease Diagnosis."

The technical reviewer for this report was David A. Hurdis (Code 2133).

The authors wish to thank Jim Donald (Code 019) for his encouragement and support of the project and Karen Holt (Code 5431) for her assistance with the technical editing. Appreciation is also extended to D. H. Wilson (Engineering Technology Center) and J. Kassal (Analysis and Technology, Inc.) for their help with the experiment.

Reviewed and Approved: 6 October 1997



Ronald J. Martin

Head, Submarine Sonar Department

REPORT DOCUMENTATION PAGE			Form Approved OMB No. 0704-0188	
Public reporting for this collection of information is estimated to average 1 hour per response, including the time for reviewing instructions, searching existing data sources, gathering and maintaining the data needed, and completing and reviewing the collection of information. Send comments regarding this burden estimate or any other aspect of this collection of information, including suggestions for reducing this burden, to Washington Headquarters Services, Directorate for Information Operations and Reports, 1215 Jefferson Davis Highway, Suite 1204, Arlington, VA 22202-4302, and to the Office of Management and Budget, Paperwork Reduction Project (0704-0188), Washington, DC 20503.				
1. AGENCY USE ONLY (Leave blank)		2. REPORT DATE 6 October 1997		3. REPORT TYPE AND DATES COVERED Final
4. TITLE AND SUBTITLE Beamformed Nearfield Imaging of a Simulated Coronary Artery Containing a Stenosis			5. FUNDING NUMBERS	
6. AUTHOR(S) Andrew J. Hull Norman L. Owsley				
7. PERFORMING ORGANIZATION NAME(S) AND ADDRESS(ES) Naval Undersea Warfare Center Division 1176 Howell Street Newport, RI 02841-1708			8. PERFORMING ORGANIZATION REPORT NUMBER TR 10,820	
9. SPONSORING/MONITORING AGENCY NAME(S) AND ADDRESS(ES) Office of Naval Research 800 North Quincy Street Arlington, VA 22217-5000			10. SPONSORING/MONITORING AGENCY REPORT NUMBER	
11. SUPPLEMENTARY NOTES				
12a. DISTRIBUTION/AVAILABILITY STATEMENT Approved for public release; distribution is unlimited.			12b. DISTRIBUTION CODE	
13. ABSTRACT (Maximum 200 words) This report describes a method that detects and localizes an artery containing a partial blockage by exploiting the shear wave field properties of the surrounding solid. An array measurement system is placed on the free surface of a urethane mold that contains a surgical tube. Inside the surgical tube is a nylon blockage that acts as a constriction to the water flowing through the tube. A turbulent field develops in and downstream of the blockage, creating a randomly fluctuating pressure on the inner wall of the tube. This force produces shear and compressional wave energy in the urethane. At low frequencies, the array is used to measure the dominant shear wave energy, and nearfield (i.e., focused) beamforming algorithms are used to detect and localize these energy emissions in the three-dimensional solid. An experiment and numerical simulations are included to demonstrate this new approach to diagnosing arterial disease.				
14. SUBJECT TERMS Arterial Disease Phased Array Technology Noninvasive Detection Beamformed Imaging Nearfield Beamforming Algorithms			15. NUMBER OF PAGES 42	
			16. PRICE CODE	
17. SECURITY CLASSIFICATION OF REPORT Unclassified	18. SECURITY CLASSIFICATION OF THIS PAGE Unclassified	19. SECURITY CLASSIFICATION OF ABSTRACT Unclassified	20. LIMITATION OF ABSTRACT SAR	

TABLE OF CONTENTS

Section	Page
1 INTRODUCTION.....	1
2 FOCUSED BEAMFORMING.....	3
3 SIMULATION.....	5
4 EXPERIMENT.....	7
5 RESULTS.....	13
6 CONCLUSIONS AND RECOMMENDATIONS.....	53
7 REFERENCES.....	55

LIST OF ILLUSTRATIONS

Figure	Page
1 Wall Pressure Versus Spatial Location.....	6
2 Urethane Mold With Embedded Surgical Tube.....	9
3 Occlusion Used in Experiment.....	10
4 Laboratory Configuration.....	10
5 Two-Dimensional Array With 1/8-Inch Surgical Tube Depicted as a Dashed Line.....	11
6 Array and Blockage Location for First Experiment.....	15
7 Simulation and Experimental Data of CFB for Experiment One at 200 Hz.....	17
8 Simulation and Experimental Data of CFB for Experiment One at 300 Hz.....	19
9 Simulation and Experimental Data of CFB for Experiment One at 400 Hz.....	21
10 Simulation and Experimental Data of CFB for Experiment One at 500 Hz.....	23
11 Simulation and Experimental Data of RVDR Focused Beamformer for Experiment One at 200 Hz.....	25

LIST OF ILLUSTRATIONS (Cont'd)

Figure	Page
12 Simulation and Experimental Data of RVDR Focused Beamformer for Experiment One at 300 Hz.....	27
13 Simulation and Experimental Data of RVDR Focused Beamformer for Experiment One at 400 Hz.....	29
14 Simulation and Experimental Data of RVDR Focused Beamformer for Experiment One at 500 Hz.....	31
15 Array and Blockage Location for Second Experiment.....	33
16 Simulation and Experimental Data of CFB for Experiment Two at 200 Hz.....	35
17 Simulation and Experimental Data of CFB for Experiment Two at 300 Hz.....	37
18 Simulation and Experimental Data of CFB for Experiment Two at 400 Hz.....	39
19 Simulation and Experimental Data of CFB for Experiment Two at 500 Hz.....	41
20 Simulation and Experimental Data of RVDR Focused Beamformer for Experiment Two at 200 Hz.....	43
21 Simulation and Experimental Data of RVDR Focused Beamformer for Experiment Two at 300 Hz.....	45
22 Simulation and Experimental Data of RVDR Focused Beamformer for Experiment Two at 400 Hz.....	47
23 Simulation and Experimental Data of RVDR Focused Beamformer for Experiment Two at 500 Hz.....	49

BEAMFORMED NEARFIELD IMAGING OF A SIMULATED CORONARY ARTERY CONTAINING A STENOSIS

1. INTRODUCTION

Coronary artery disease (CAD) is a primary precursor of heart attacks, the leading cause of death in the United States. CAD is the buildup of plaque in the coronary arteries resulting in a condition referred to as stenosis in which blood flow is restricted and the oxygen supply to the heart muscle is decreased. The end result of arterial stenosis is frequently myocardial infarction and subsequent necrosis (i.e., permanent heart muscle damage). Presymptomatic detection of coronary stenosis before heart damage has occurred is extremely important because the disease could be treated with diet and drugs rather than with coronary bypass surgery or angioplasty. Early CAD diagnosis on a wide scale would save the U.S. health care system billions of dollars and would allow a much better quality of life to those who suffer from heart disease.

The most common method to measure blood flow and stenosis in coronary arteries is by an invasive test called an angiogram. During this procedure, a catheter injects a radiopaque substance into the coronary arteries, while an x-ray screen simultaneously reveals the arterial blockages of the patient to the doctor. However, an angiogram is costly and places the patient at significant risk. For many years, a nonintrusive method called ultrasound has been used by cardiologists to image the coronary valves. This technique, which exploits the compressional wave field in the human body, typically uses an actuator to emit low-level energy into the body where it is absorbed and reflected to varying degrees. An accompanying array of sensors receives the energy back and an image is formed with a volume-scanning focused beamformer. Although ultrasound can also image the inside of a near-surface artery, such as the carotid artery, it cannot image a coronary artery due to its depth, its smaller size, and the nearby scattering of energy.

In this report, a new method that is proposed to detect and localize arterial stenoses uses the shear wave space-time field of a solid body and phased array technology to image the underlying volume.¹ The approach is based on the turbulent normal wall forces that are present in and downstream from a stenosis.^{2,3} These wall forces, while extremely small, exert a pressure on the wall of the artery, which causes a displacement in the surrounding soft tissue. This displacement occurs in the form of two elastic waves in the medium: a compressional

wave and a shear wave. At low frequencies (100 to 500 Hz), the shear wave dominates the response and can be measured at the surface of the solid by an array of sensors. Then, nearfield (focused) beamforming imaging algorithms allow detection and localization of the stenosis. An *in vitro* experiment is included to validate this method and corresponding simulations are presented.

2. FOCUSED BEAMFORMING

The beamformer is defined by assuming that $\mathbf{x}(\omega_0)$ is a zero-mean, stationary, complex vector of N random sensor outputs that are Fourier transformed at fixed frequency ω_0 . The image scalar pixel value of the conventional focused beamformer (CFB) at Cartesian coordinates x_i , y_i , and z_i is expressed by

$$\hat{c}(x_i, y_i, z_i, \omega_0) = \frac{\mathbf{d}(x_i, y_i, z_i, \omega_0)^H \mathbf{R}(\omega_0) \mathbf{d}(x_i, y_i, z_i, \omega_0)}{\mathbf{d}(x_i, y_i, z_i, \omega_0)^H \mathbf{d}(x_i, y_i, z_i, \omega_0)} . \quad (1)$$

In equation (1), $\mathbf{R}(\omega_0) = E[\mathbf{x}(\omega_0) \mathbf{x}(\omega_0)^H]$ is the N -by- N cross-spectral density matrix (CSDM), $E[\]$ is the statistical expectation operator, and $\mathbf{d}(x_i, y_i, z_i, \omega_0)$ is the N -by-1 focused imaging vector with the n th row expressed as

$$d_n(x_i, y_i, z_i, \omega_0) = \frac{1}{[r_i(n)]^\beta} \exp\left[\frac{-j\omega_0 r_i(n)}{c}\right], \quad (2)$$

where β is the geometric spreading loss factor, c is the average wave speed, and $r_i(n)$ is the apparent Euclidean distance from the i th image point to the n th sensor located at $x(n)$, $y(n)$, and $z(n)$. This Euclidean distance is expressed as

$$r_i(n) = \sqrt{[x_i - x(n)]^2 + [y_i - y(n)]^2 + [z_i - z(n)]^2} . \quad (3)$$

In addition, the image scalar pixel value of the reduced variance distortionless response (RVDR) focused beamformer at Cartesian coordinates x_i , y_i , and z_i and at fixed frequency ω_0 is defined by

$$\hat{m}(x_i, y_i, z_i, \omega_0) = \frac{\mathbf{w}(x_i, y_i, z_i, \omega_0)^H \mathbf{R}(\omega_0) \mathbf{w}(x_i, y_i, z_i, \omega_0)}{\mathbf{w}(x_i, y_i, z_i, \omega_0)^H \mathbf{w}(x_i, y_i, z_i, \omega_0)} , \quad (4)$$

where $\mathbf{w}(x_i, y_i, z_i, \omega_0)$ is the N -by-1 focused minimum variance distortionless response (MVDR) sensor array filter vector. This vector is expressed as

$$\mathbf{w}(x_i, y_i, z_i, \omega_0) = \hat{\mathbf{R}}(\omega_0)^{-1} \mathbf{d}(x_i, y_i, z_i, \omega_0) , \quad (5)$$

where $\mathbf{d}(x_i, y_i, z_i, \omega_0)$ is given in equation (2) and $\hat{\mathbf{R}}(\omega_0)$ is the diagonal enhanced CSDM defined by

$$\hat{\mathbf{R}}(\omega_0) = \mathbf{R}(\omega_0) + e \left\{ \frac{\text{Trace}[\mathbf{R}(\omega_0)]}{N} \right\} \mathbf{I} , \quad (6)$$

where e is the scalar enhancement factor and \mathbf{I} is the N -by- N identity matrix. It is noted that if e equals infinity, equation (4) becomes a conventional beamformer, and if e equals zero, equation (4) becomes an MVDR beamformer.⁴

3. SIMULATION

Numerical simulation of this problem consists of analytically formulating the CSDM, inserting it into equations (1) and (4), and then calculating the simulated beamformed image. The analytical model of the turbulent flow energy, based on previous laboratory wall pressure measurements downstream of a blockage,³ is modified to include energy in the region of the blockage. Additionally, a spatial correlation term is added to the model to account for the spatial coherence of the turbulent flow.⁵ The expression for the streamwise wall pressure autospectrum is given as

$$P(x, \omega_0) = p(x) \exp\left(\frac{\gamma |x| \omega_0}{U_c}\right) \exp\left(\frac{j \omega_0 x}{U_c}\right), \quad (7)$$

where $p(x)$ is the amplitude of the wall pressure shown in figure 1, x is the streamwise location of the flow measured from a reference point (m), γ is the spatial decay constant (dimensionless), and U_c is the fluid convection speed (m/s). In figure 1, the ordinate is the root mean square (rms) wall pressure nondimensionalized by the fluid density ρ , the square of the constriction velocity u_j , the constricted diameter d , and the unconstricted diameter D ; the abscissa is the spatial location x . For this study, the spatial decay constant was -0.125 and the fluid convection speed was the flow velocity through the constricted portion of the tube. Equation (7) is used to form the M -by- M CSDM $\mathbf{E}(\omega_0)$ of the source (blockage and downstream energy), which has the element in the u th row and v th column expressed as

$$E_{uv}(\omega_0) = \begin{cases} \frac{p(x_u)p(x_v)}{\{\max_x[p(x)]\}^2} \exp\left(\frac{\gamma |x_u - x_v| \omega_0}{U_c}\right) \exp\left(\frac{j \omega_0 (x_u - x_v)}{U_c}\right), & u \leq v \\ \frac{p(x_u)p(x_v)}{\{\max_x[p(x)]\}^2} \exp\left(\frac{\gamma |x_u - x_v| \omega_0}{U_c}\right) \exp\left(\frac{j \omega_0 (x_v - x_u)}{U_c}\right), & v < u \end{cases} \quad (8)$$

For the source model used here, the indices u and v range from 1 to 21 and correspond to the circled data points in figure 1, and $\max_x[p(x)]$ is the maximum value of the pressure with respect to spatial location x . Once this matrix is known, the simulated CSDM can be determined using

$$\mathbf{R}(\omega_0) = \sigma_s^2 \left\{ \frac{N}{\text{Trace}[\mathbf{D}(\omega_0) \mathbf{E}(\omega_0) \mathbf{D}^H(\omega_0)]} \right\} \mathbf{D}(\omega_0) \mathbf{E}(\omega_0) \mathbf{D}^H(\omega_0) + \sigma_0^2 \mathbf{I}, \quad (9)$$

where $\mathbf{D}(\omega_0)$ is the N -by- M matrix from the n th sensor to the u th source whose n uth element is expressed as

$$D_{nu}(\omega_0) = \frac{1}{[l(n,u)]^\beta} \exp\left[\frac{-j\omega_0 l(n,u)}{c}\right], \quad (10)$$

where $l(n,u)$ is the Euclidean distance from the n th sensor to the u th source, given as

$$l(n,u) = \sqrt{[x(n) - x(u)]^2 + [y(n) - y(u)]^2 + [z(n) - z(u)]^2}; \quad (11)$$

σ_0^2 is the spectral density of the zero-mean spatially uncorrelated additive noise at each sensor; and σ_s^2 is the signal at the peak of the spatial spectrum.

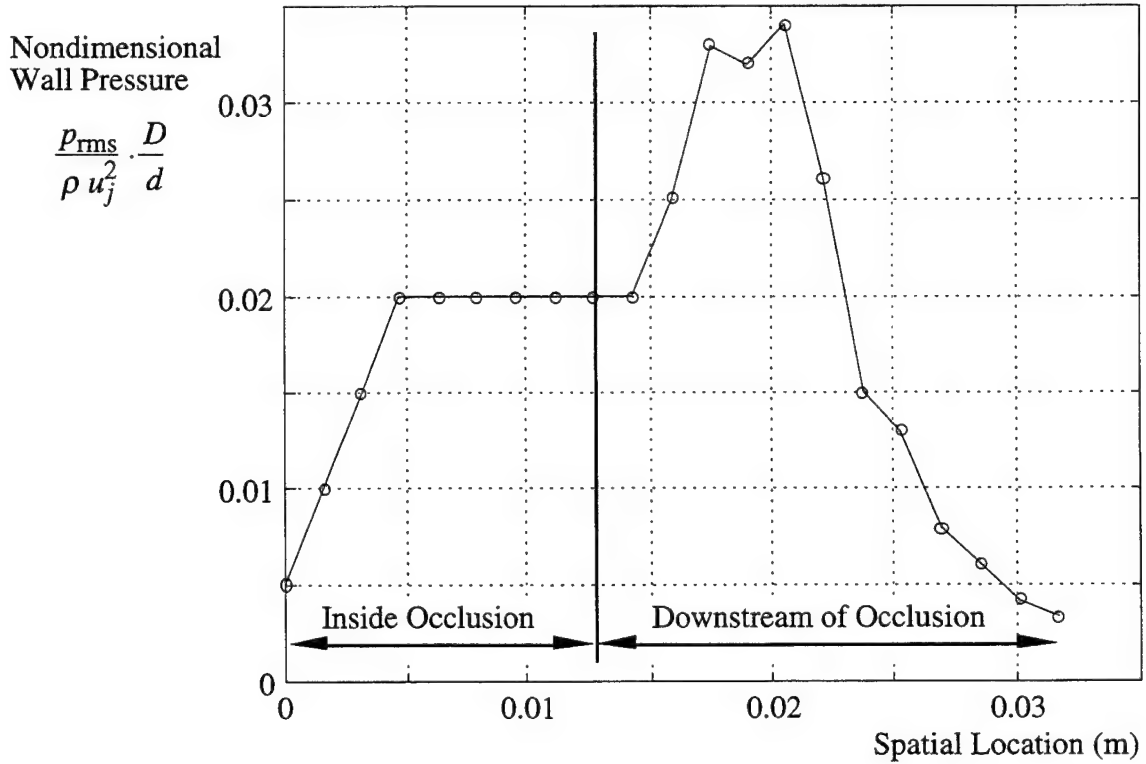


Figure 1. Wall Pressure Versus Spatial Location

4. EXPERIMENT

A homogeneous urethane mold containing a latex surgical tube was manufactured for the *in vitro* tests, as shown in figure 2. The surgical tube, intended to simulate the mid left anterior descending coronary artery, has an inner diameter of 0.00318 m (0.125 in.) and is embedded at a depth of 0.0318 m (1.25 in.) in the urethane. The urethane, which is Hexcel 195-RE, represents the surrounding soft tissue and has a shear wave speed of 7 m/s at 100 Hz and 12 m/s at 1000 Hz. The 100- to 1000-Hz shear wave speed is approximated by using a linear dispersion relationship with respect to frequency. (It should be noted here that the slowest shear wave speed available in a commercial grade urethane is somewhat faster than soft human tissue shear wave speed at low frequencies.⁶) The surgical tube contains a flow blockage (nylon), which represents a coronary (partial) occlusion having a length of 0.0127 m (0.5 in.) and a hole with an inner diameter of 0.00159 m (0.0625 in.), as shown in figure 3. This blockage was chosen because it has a 50-percent diameter reduction (or a 75-percent area reduction), which is similar to the reduction used by other researchers who have measured break frequencies,⁷ velocity,⁸⁻¹⁰ and pressure^{3,11,12} caused by a constriction in a cylindrical tube. The in-flow end of the nylon occlusion contains a 45-degree taper to provide a relatively smooth entrance region.

Water is gravity fed into the surgical tube from a holding tank and captured below the urethane mold in a calibrated flask, as shown in figure 4. Although this is a steady-state flow experiment, it has been shown that the force levels are nearly identical to a corresponding pulsatile flow experiment.¹² This technique permits measurement of the flow velocity from which the corresponding Reynolds numbers based on obstructed and unobstructed diameters can be computed. The moving fluid transmits a relatively small normal force into the embedded tube, which, in turn, transmits energy into the urethane. This energy propagates to the surface of the mold, primarily in the form of shear waves, where it produces a local displacement field that fluctuates in space and time. A polyvinylidene fluoride (PVDF) sensor array is used to measure this field and the beamformer is used to localize the energy emissions in the three-dimensional solid. The experiment was conducted in an electromagnetically (EM) shielded anechoic chamber to minimize ambient noise contamination.

All of the measurements in this report were taken with a two-dimensional array that consists of 15 sensors (elements) on two orthogonal axes, as shown in figure 5. A common middle sensor is shared by the nine sensors (equally spaced) on the primary axis and the seven sensors (not equally spaced) on the secondary axis. The element-to-element midpoint spacing on all of the primary axis sensors is 0.00953 m (0.375 in.). The element-to-element midpoint

spacing of each of the outer three sensors on the secondary axis is also 0.00953 m (0.375 in.), and the distance from the center sensor to its adjacent sensor is 0.0286 m (1.125 in.). Each group of three outboard sensors on the secondary orthogonal axis is built into a separate box that is attached to the main box by hinges so that the array can conform to nonplanar surfaces. A coordinate system is chosen such that the primary axis is the x -axis and the secondary axis is the z -axis. The y -axis is the image depth of the urethane block. The coordinate system origin is the intersection of the primary and the secondary array axes.

The sensing elements of the array are PVDF film strips that are 0.0381 m (1.50 in.) long and approximately 0.00927 m (0.365 in.) wide. Attached to the middle of each strip is a nearly circular piece of plastic, which has a 0.00927-m (0.365-in.) approximate diameter and a 0.00159-m (0.0625-in.) thickness. This plastic contact piece is the sensing area of the element and is used to facilitate an omnidirectional response at the short wavelengths that occur at the slow wave speeds and corresponding frequencies involved in this study.

The array elements were connected to a 20-channel low-noise preamplifier with lightweight multistrand coaxial cables (Cooner Corporation). The signals were then passed to a bank of amplifiers (Ithaco Model 451) with the low-frequency rolloff set to 1000 Hz and then to a multichannel programmable filter (Precision Filter) with the high-frequency cutoff set to 800 Hz. Finally, the signals were passed to a data acquisition system (LabView) residing in a computer (Apple Power Macintosh 8100/100) where the time series data were stored for post processing.

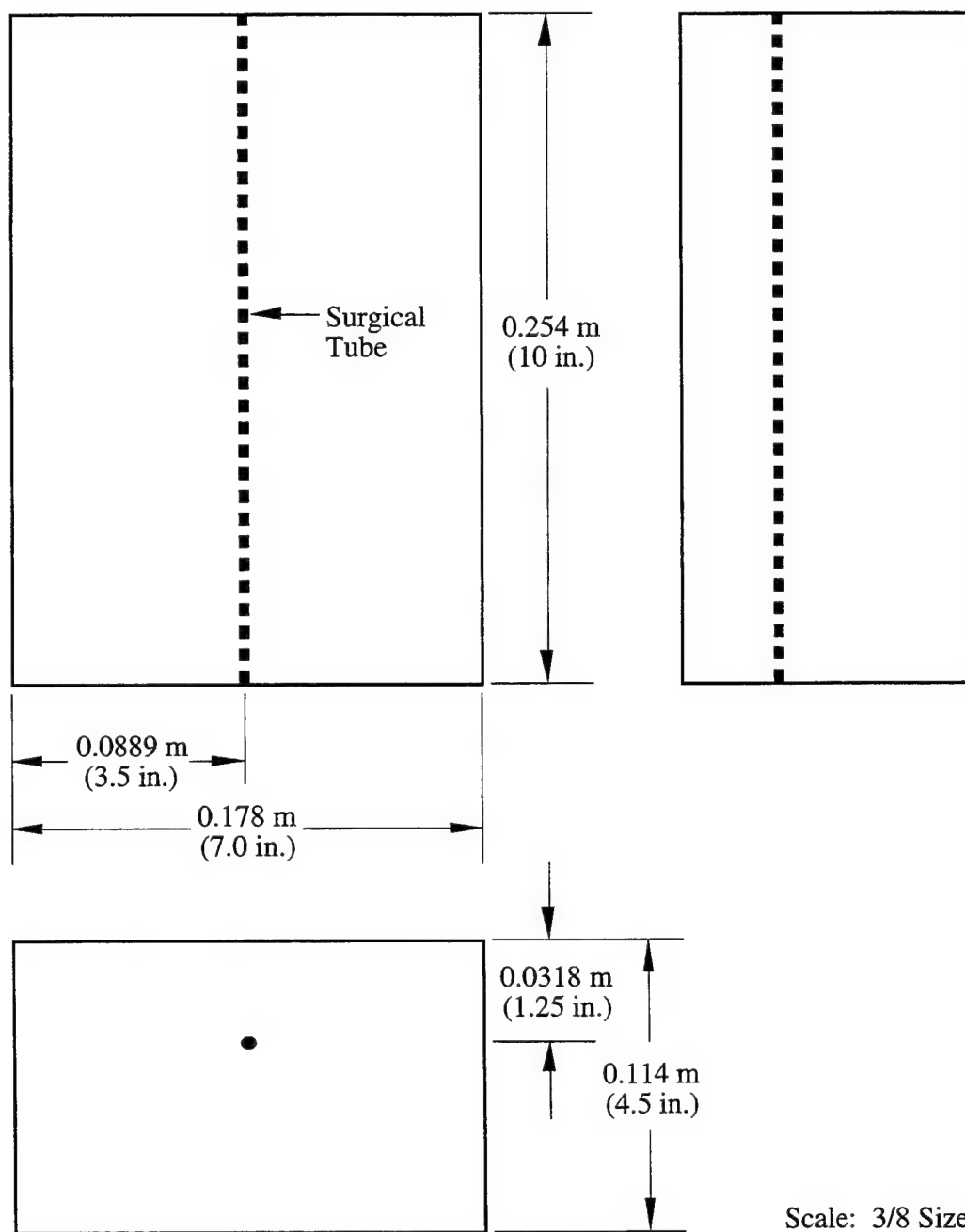


Figure 2. Urethane Mold With Embedded Surgical Tube

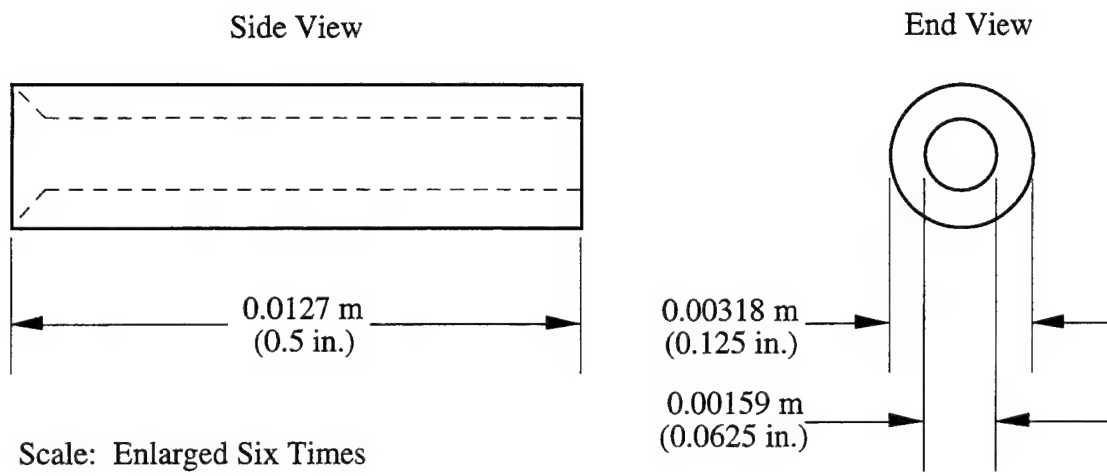


Figure 3. Occlusion Used in Experiment

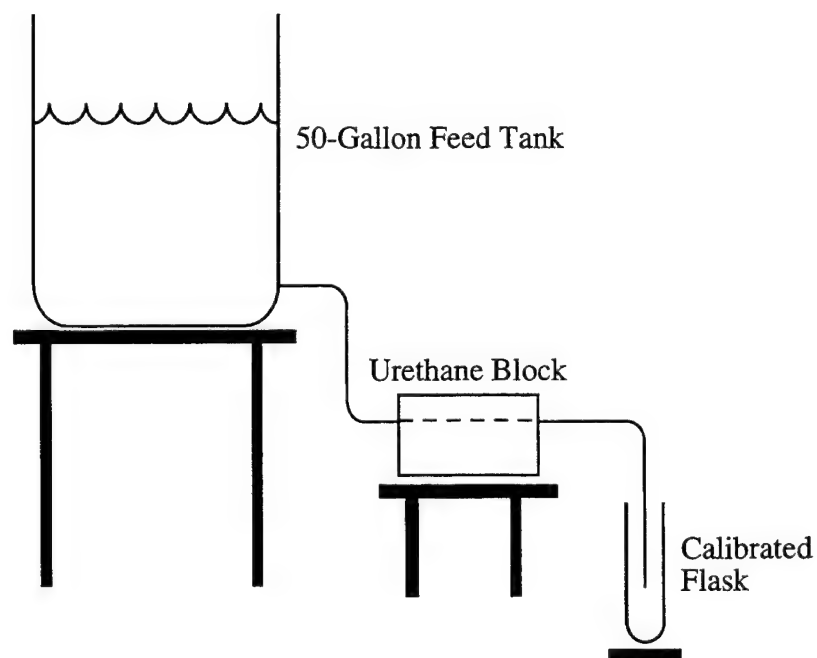
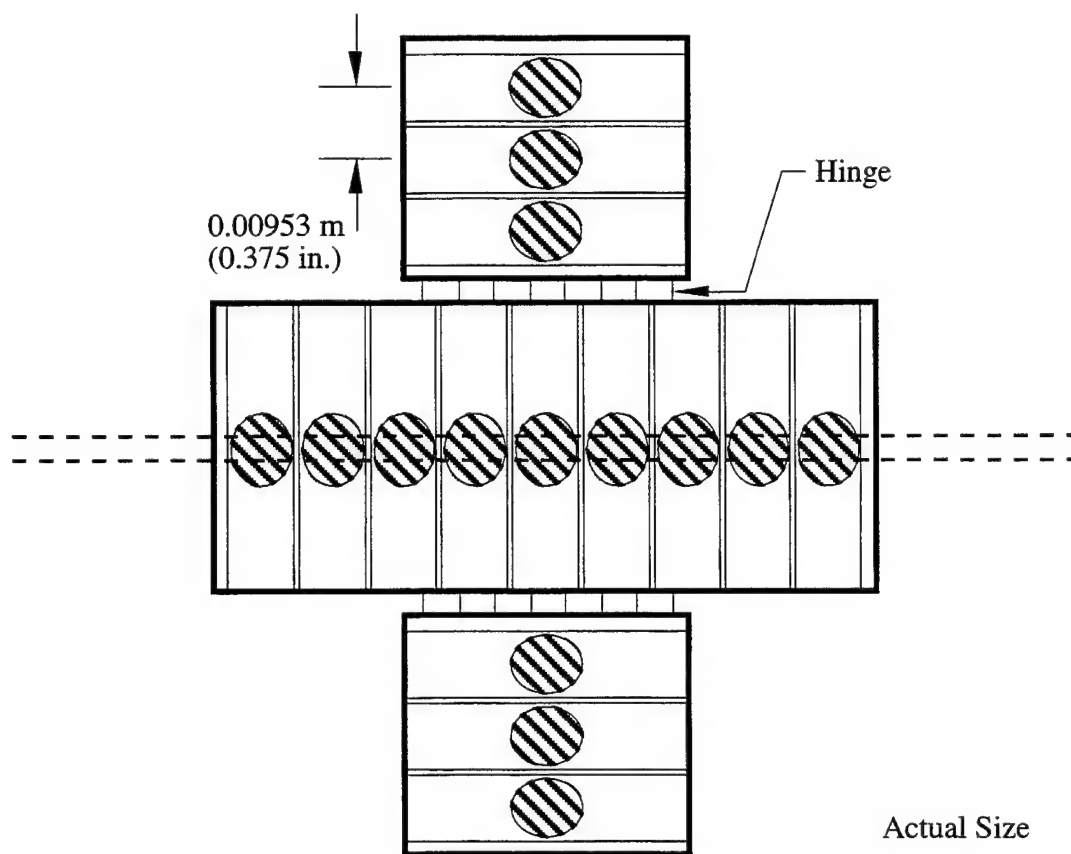


Figure 4. Laboratory Configuration



*Figure 5. Two-Dimensional Array With 1/8-Inch Surgical Tube
Depicted as a Dashed Line*

5. RESULTS

Two different geometrical configurations were numerically modeled and corresponding experimental measurements were conducted to validate the models. The first is an ideal case where the main axis of the array is parallel to the surgical tube and the middle sensor is directly over the occlusion, as shown in figure 6. Figures 7, 8, 9, and 10 are comparisons of the simulation and the data for 200, 300, 400, and 500 Hz with the CFB. Figures 11, 12, 13, and 14 are comparisons of the simulation and the data for 200, 300, 400, and 500 Hz with the RVDR focused beamformer. All the surfaces are normalized such that the maximum value is 0 dB. The experimental data were computed with 48 fast Fourier transforms that were each 1024 data points long; the sampling frequency was 2016 Hz per channel, which corresponds to a frequency bin resolution of 1.969 Hz. The wave speed used to compute all the images was linearly interpolated for each specific frequency with a value of 7 m/s at 100 Hz and 12 m/s at 1000 Hz. This resulted in a wave speed of 7.56 m/s at 200 Hz, 8.11 m/s at 300 Hz, 8.67 m/s at 400 Hz, and 9.22 m/s at 500 Hz. The spreading parameter β was 1, which represents spherical spreading at each source location and the RVDR enhancement factor was 2. The Reynolds number in the surgical tube (Re_D) was 1790 and the fluid velocity was 0.57 m/s. The Reynolds number through the constriction (Re_d) was 3580 and the fluid velocity was 2.28 m/s. It is noted that the effective constricted diameter (the vena contracta) is slightly smaller than the actual constricted diameter.¹³ Numerical simulations with smaller constricted diameters produced the same results as those using the actual constricted diameter.

In figures 7 through 14, the x -axis represents the coordinate that is parallel to the main array axis with the middle sensor centered at $x = 0$. The y -axis is image depth into the solid. The two parallel black lines centered at $y = 3.18$ cm on figures 7 through 14 represent the surgical tube in the urethane. The solid black rectangle centered at $x = 0$ and $y = 3.18$ cm is the occlusion. The fluid is flowing from the right side of the image to the left side. The yellow rectangles at $y = 0$ depict the sensor location on the main axis of the array. The sensors on the secondary axis of the array are not shown. The color bar on the right-hand side of each image is the scale of the image in decibels. The minimum surface value plotted is -10 dB.

The second geometrical configuration is the case where the main axis of the array is orthogonal to the surgical tube and the blockage is between two of the sensors of the array. Shown in figure 15, this is representative of a human test where an artery with an occlusion is at some unknown location. Figures 16, 17, 18, and 19 are comparisons of the simulation and the data for 200, 300, 400, and 500 Hz with the CFB, and figures 20, 21, 22, and 23 are comparisons of the simulation and the data for 200, 300, 400, and 500 Hz with the RVDR

focused beamformer. The Reynolds number in the surgical tube (Re_D) was 1820 and the fluid velocity was 0.58 m/s. The Reynolds number through the constriction (Re_d) was 3640 and the fluid velocity was 2.32 m/s. The simulated and experimental constants used in the first case were also used in this one.

In figures 15 through 23, the x -axis represents the coordinate that is parallel to the main array axis with the middle sensor centered at $x = 0$. The y -axis is image depth into the solid. The arrow-marked black circle centered at $y = 3.18$ cm and $x = 2.38$ cm on figures 16 through 23 represents the surgical tube in the urethane. The fluid is flowing up and out of the image and is orthogonal to the image plane. The yellow rectangles at $y = 0$ depict the sensor location on the main axis of the array. The sensors on the secondary axis of the array are not shown. The color bar on the right-hand side of the images is the scale of the image in decibels. The minimum surface value plotted is -10 dB.

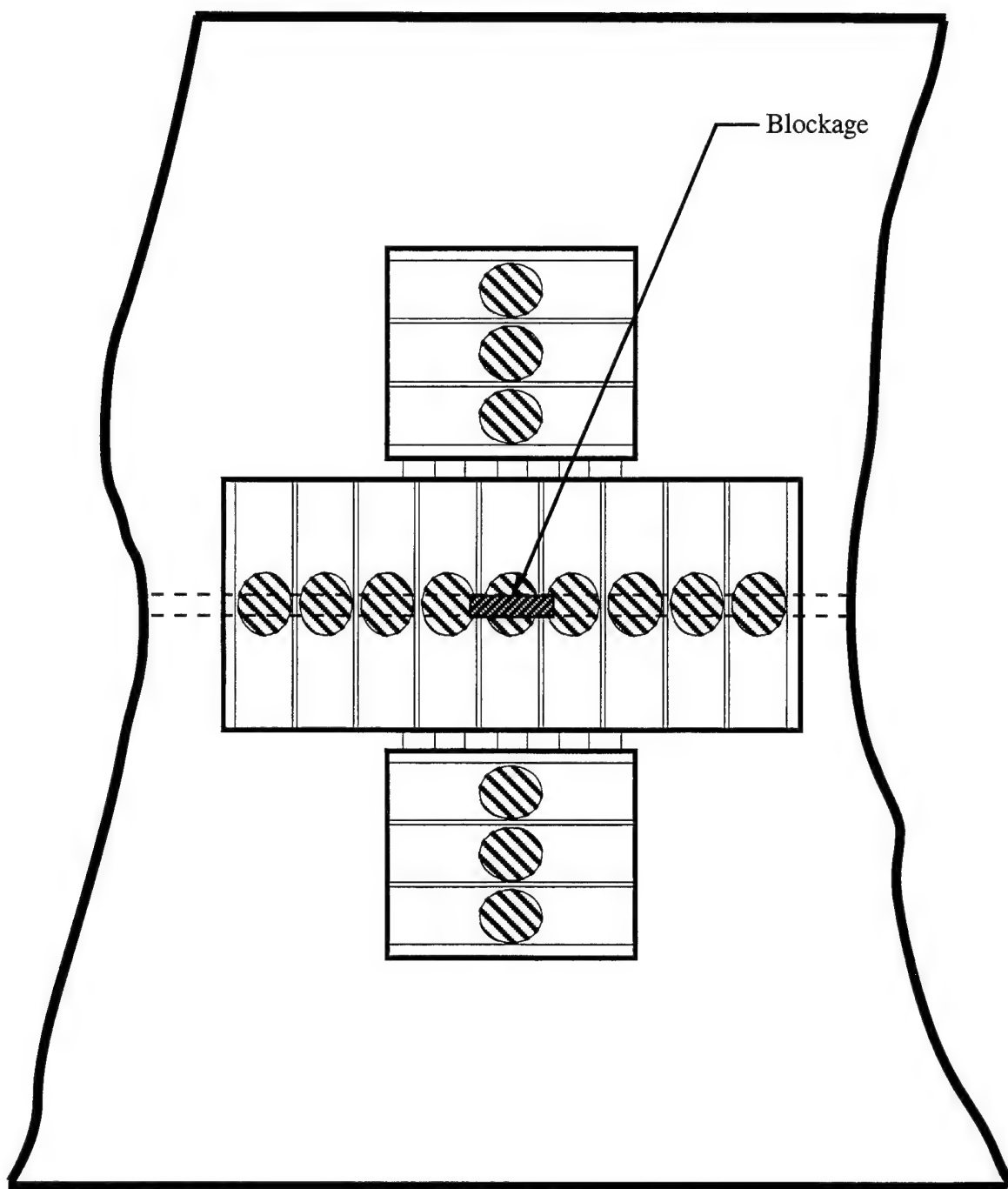


Figure 6. Array and Blockage Location for First Experiment

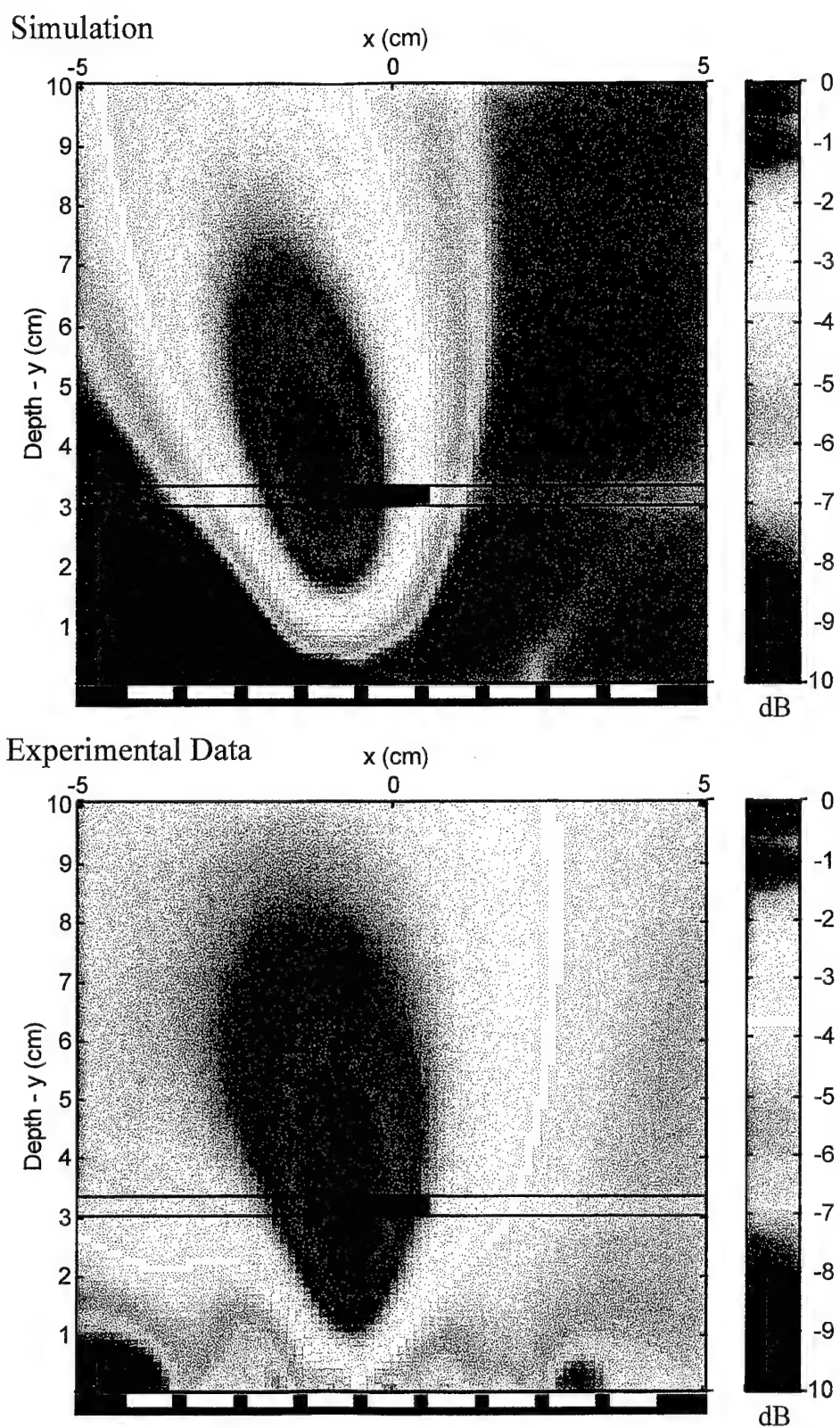


Figure 7. Simulation and Experimental Data of CFB for Experiment One at 200 Hz

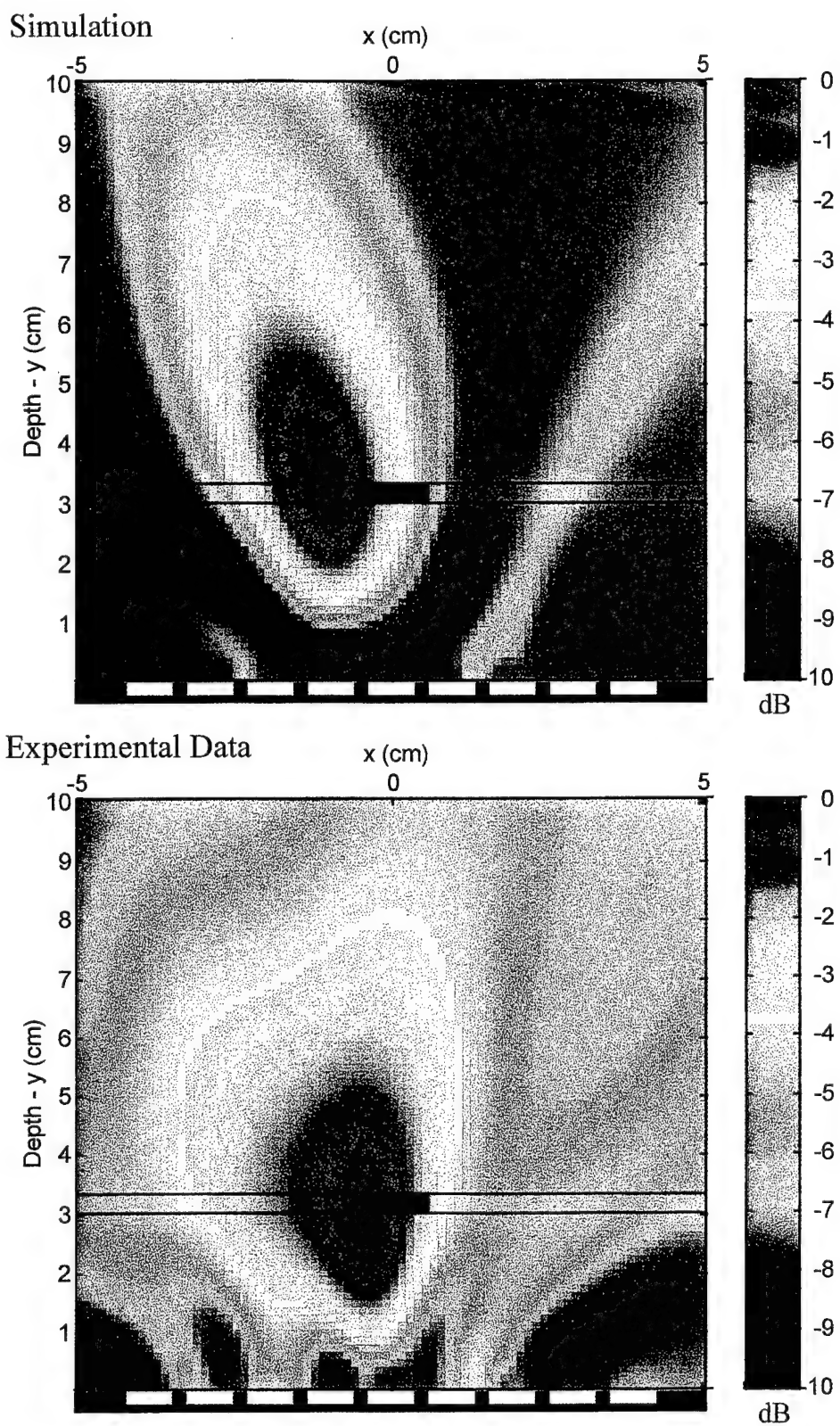


Figure 8. Simulation and Experimental Data of CFB for Experiment One at 300 Hz

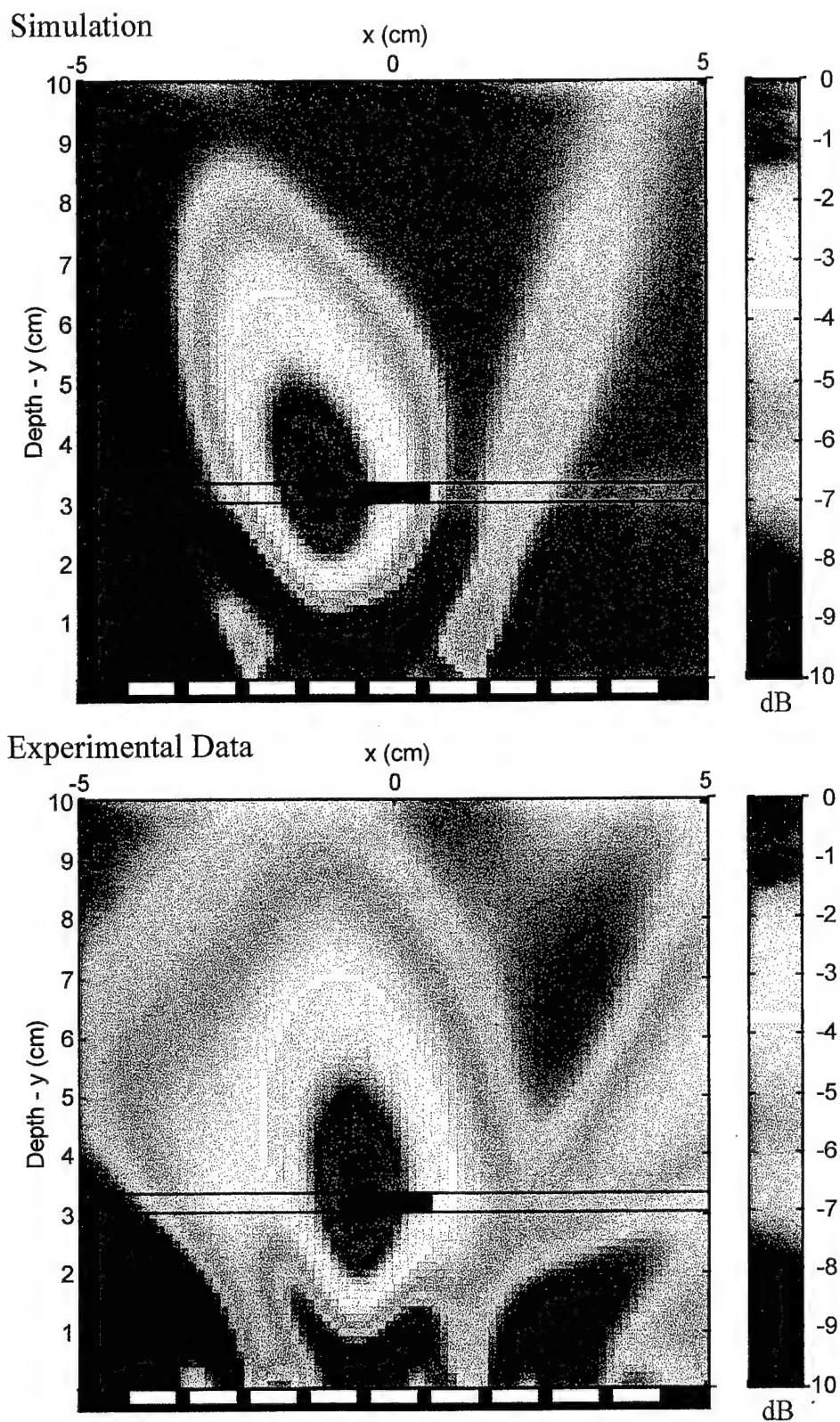


Figure 9. Simulation and Experimental Data of CFB for Experiment One at 400 Hz

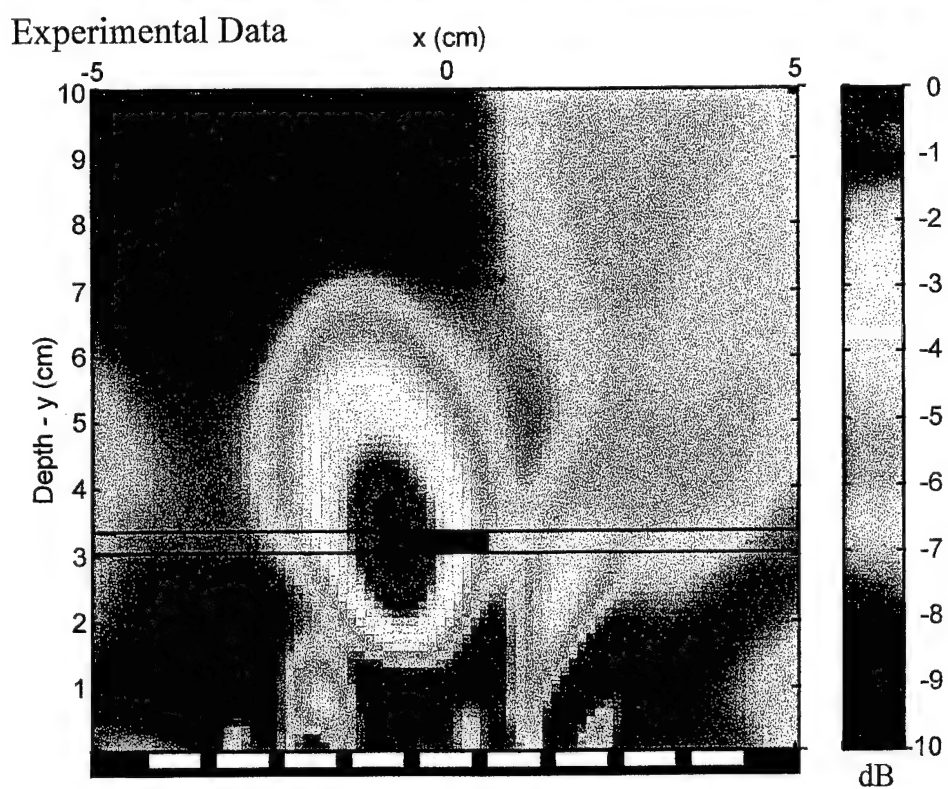
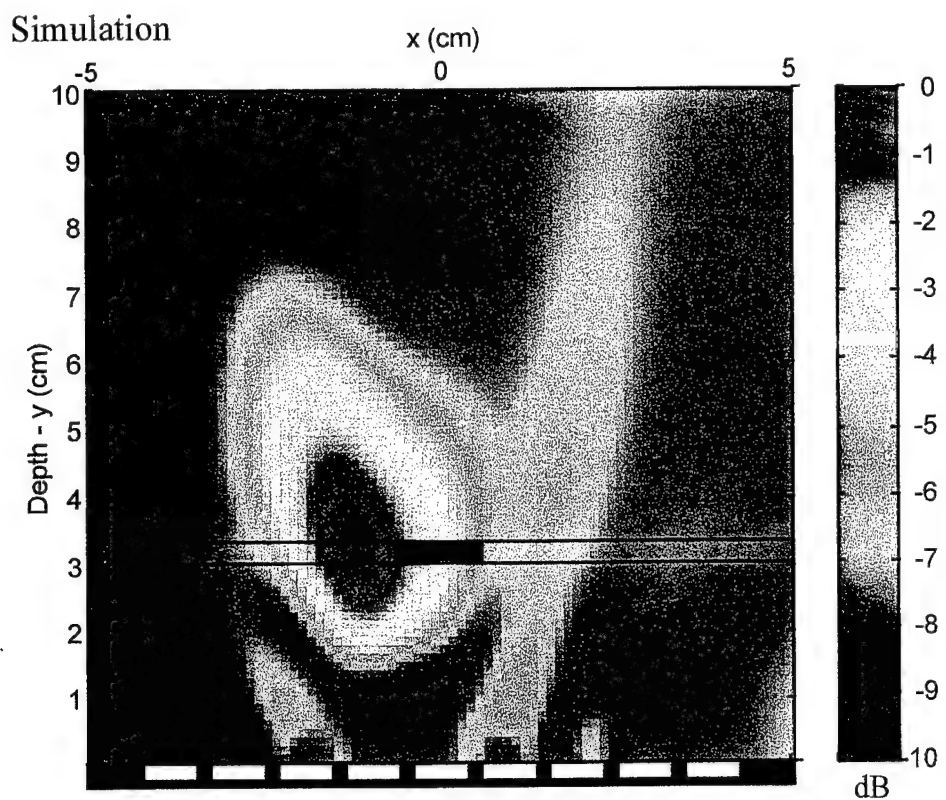


Figure 10. Simulation and Experimental Data of CFB for Experiment One at 500 Hz

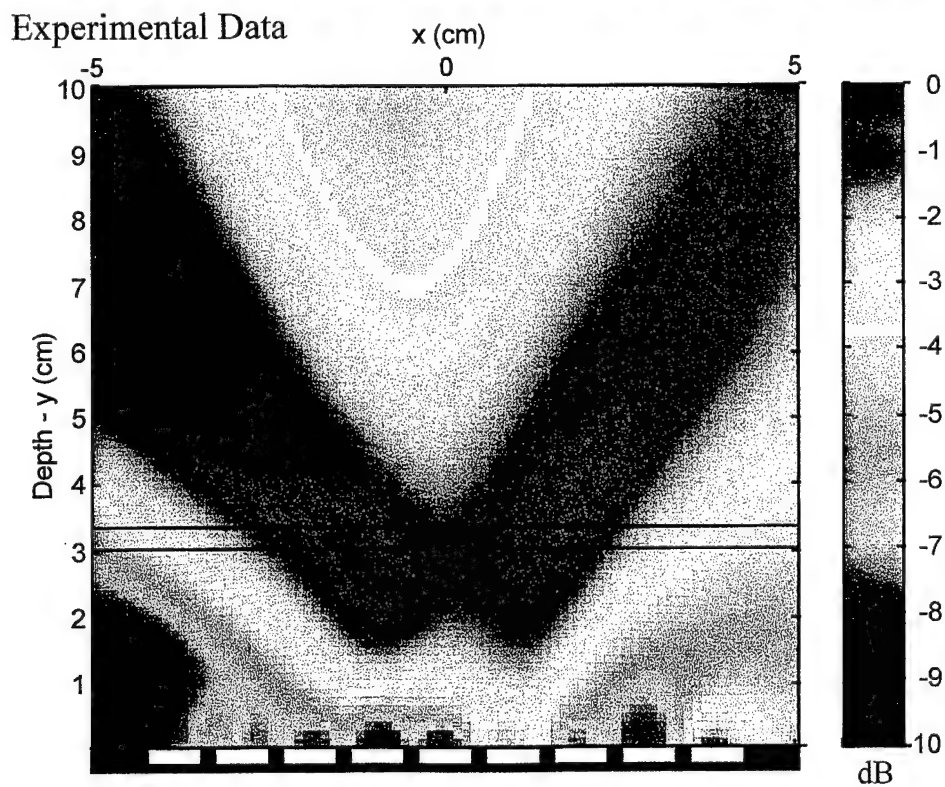
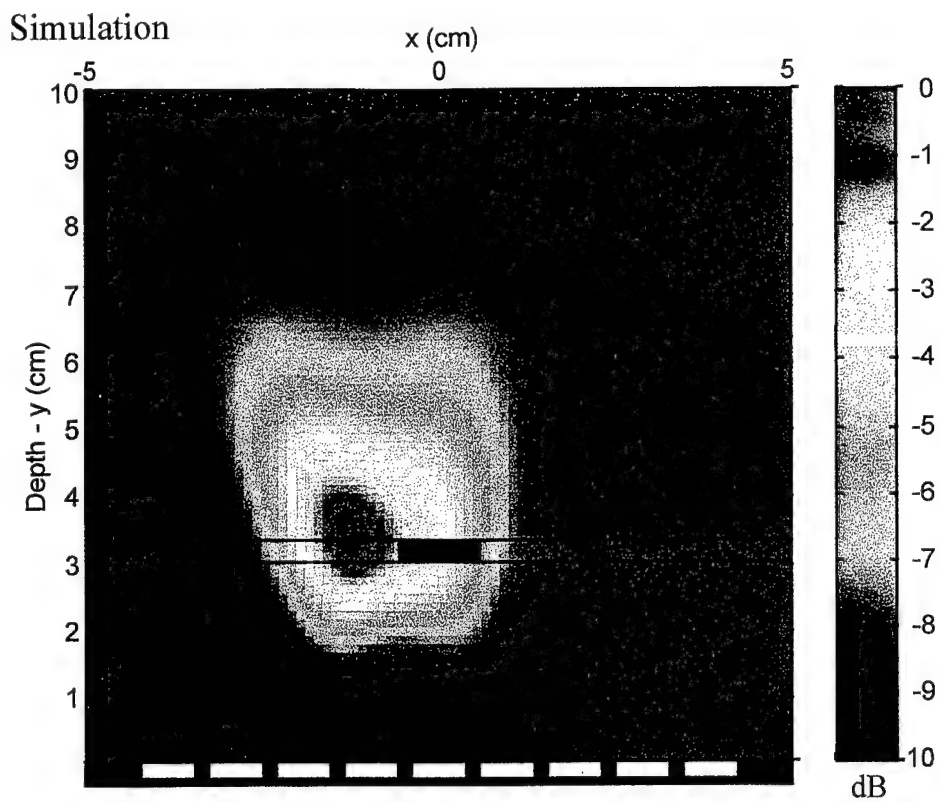


Figure 11. Simulation and Experimental Data of RVDR Focused Beamformer for Experiment One at 200 Hz

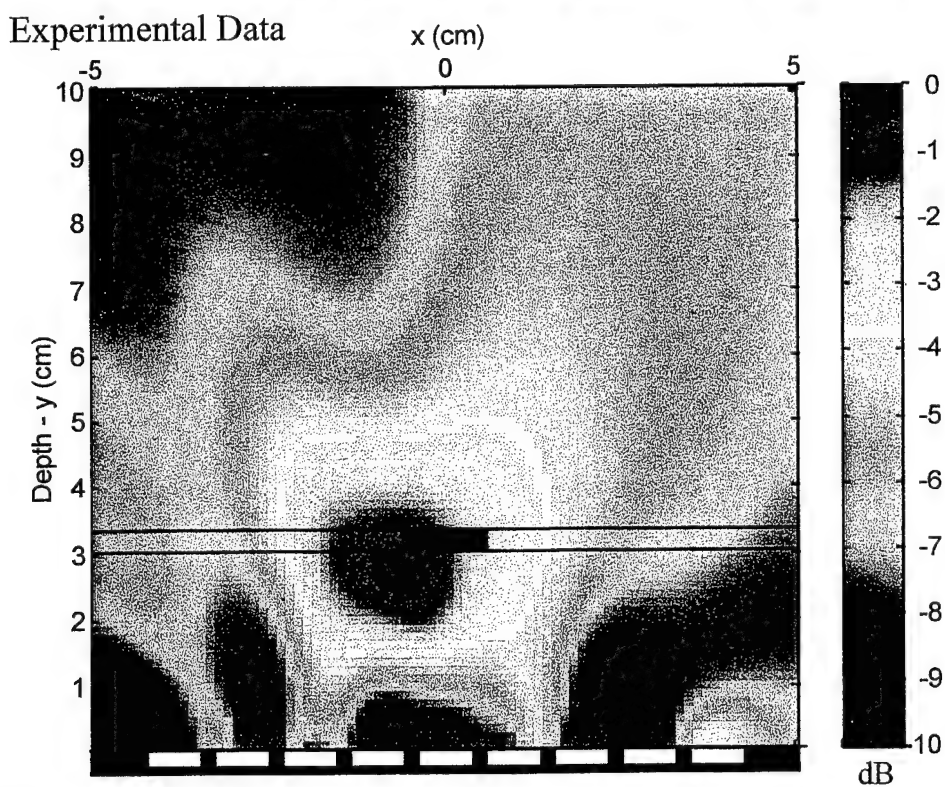
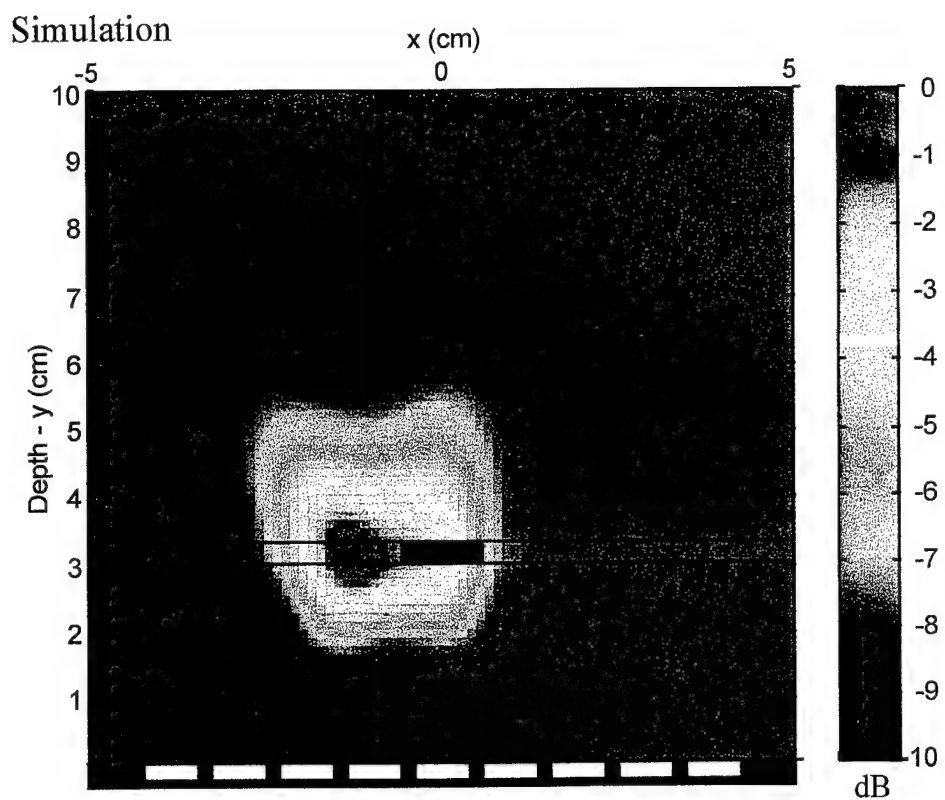


Figure 12. Simulation and Experimental Data of RVDR Focused Beamformer for Experiment One at 300 Hz

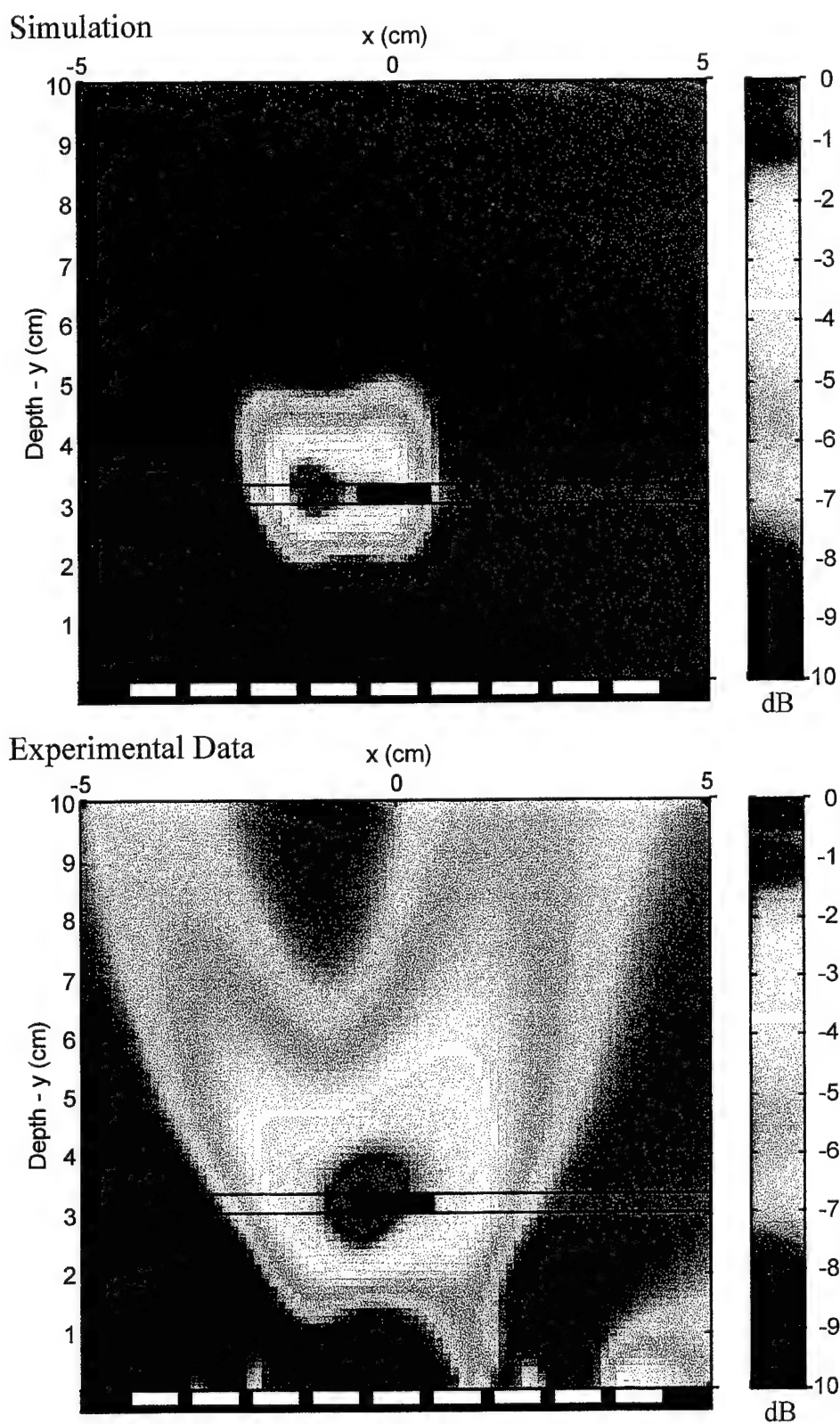


Figure 13. Simulation and Experimental Data of RVDR Focused Beamformer for Experiment One at 400 Hz

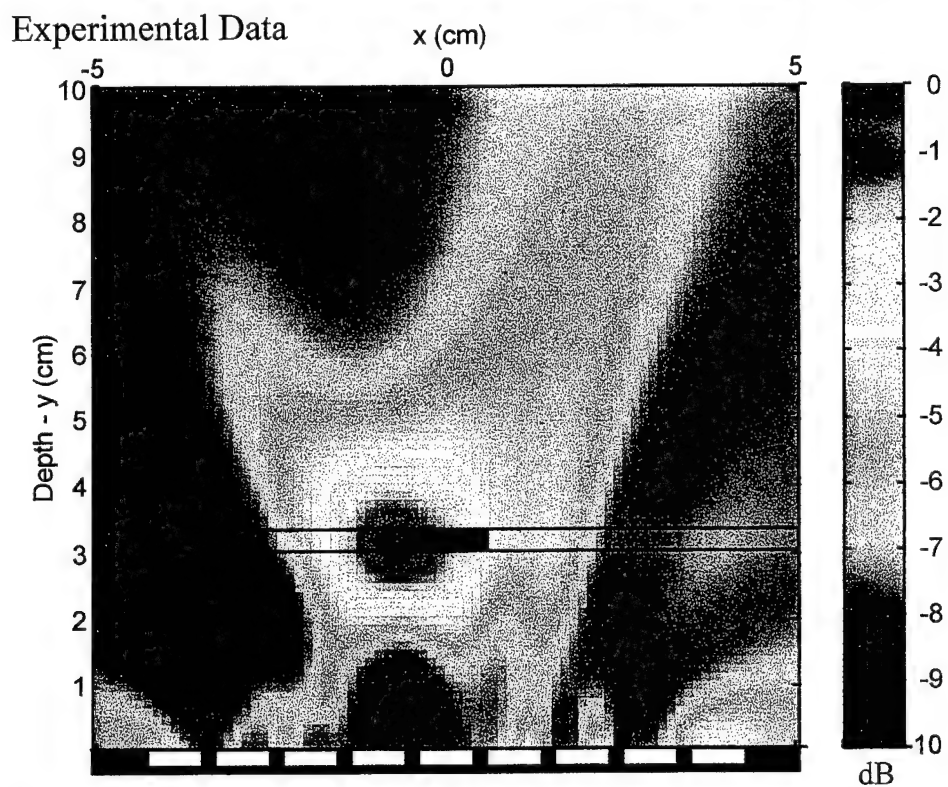
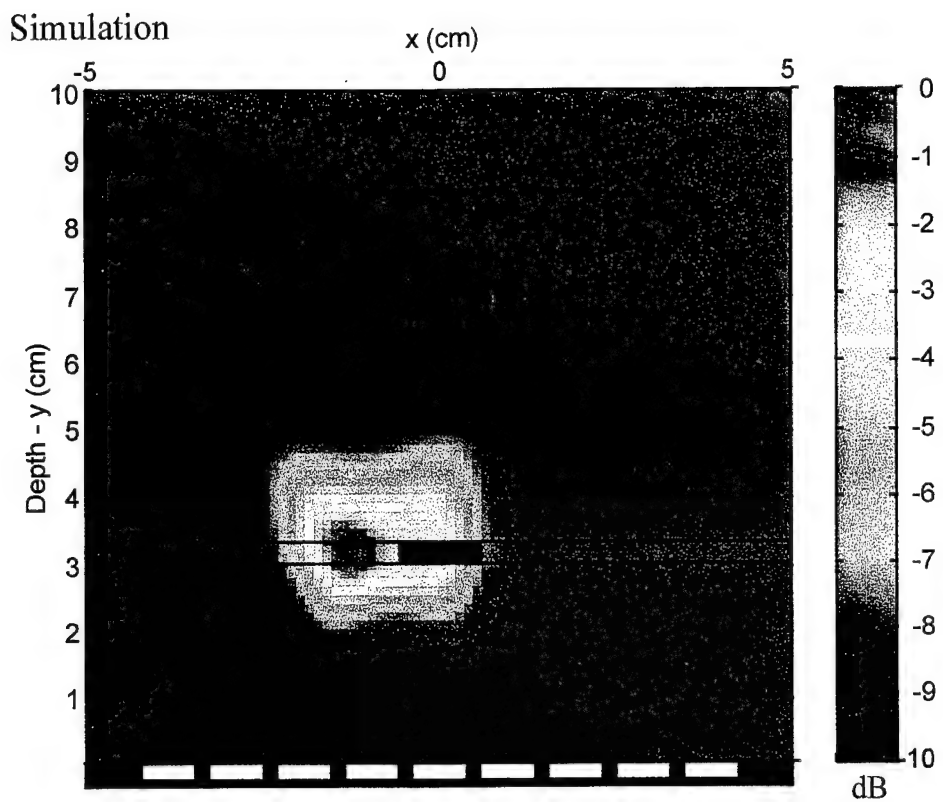


Figure 14. Simulation and Experimental Data of RVDR Focused Beamformer for Experiment One at 500 Hz

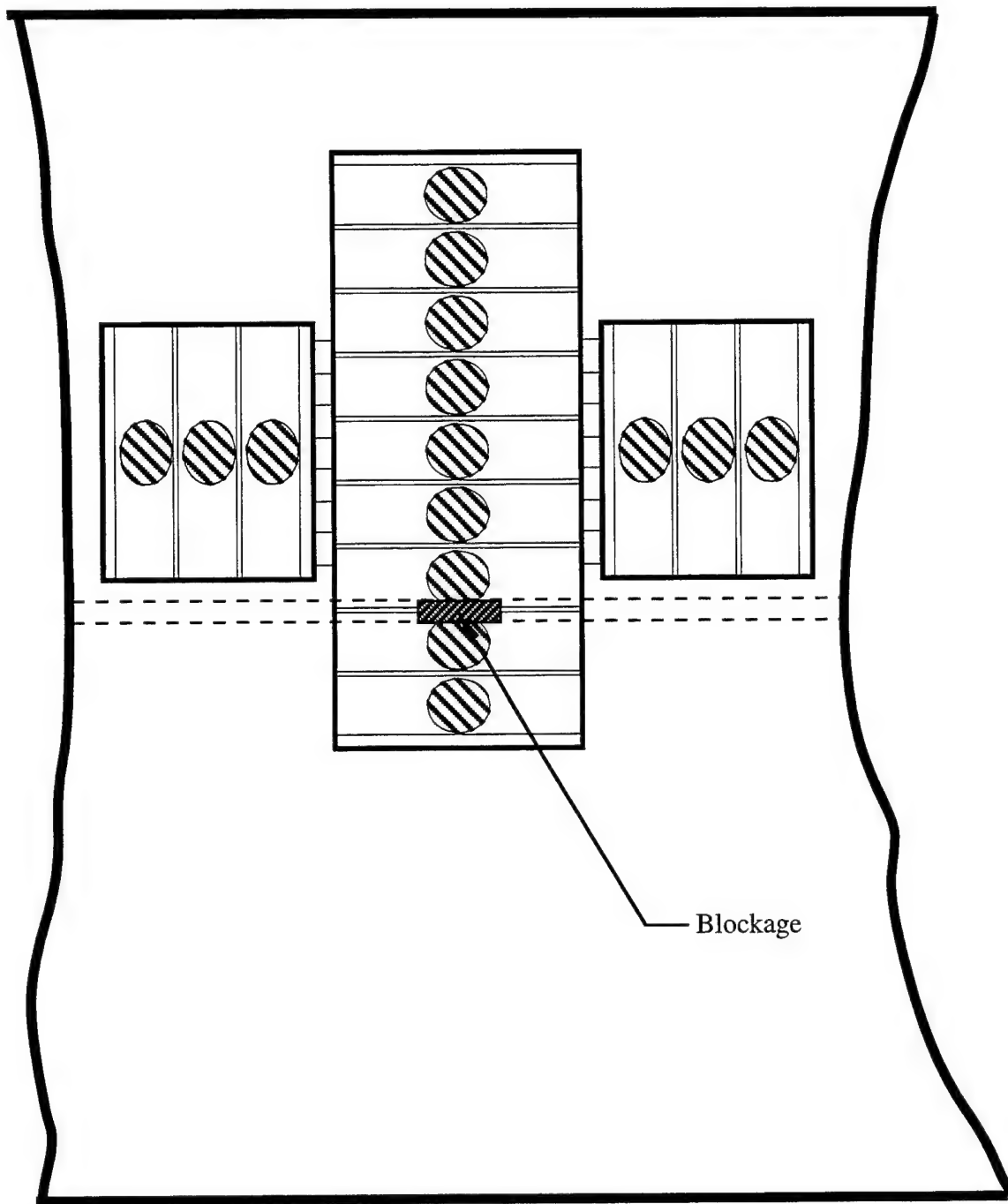


Figure 15. Array and Blockage Location for Second Experiment

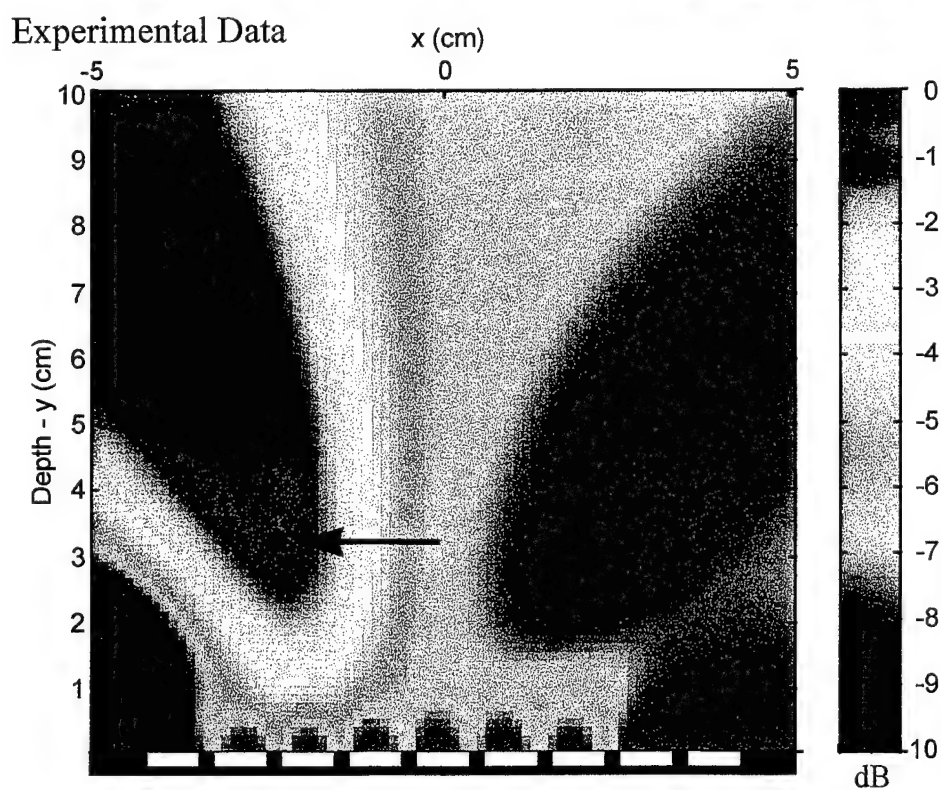
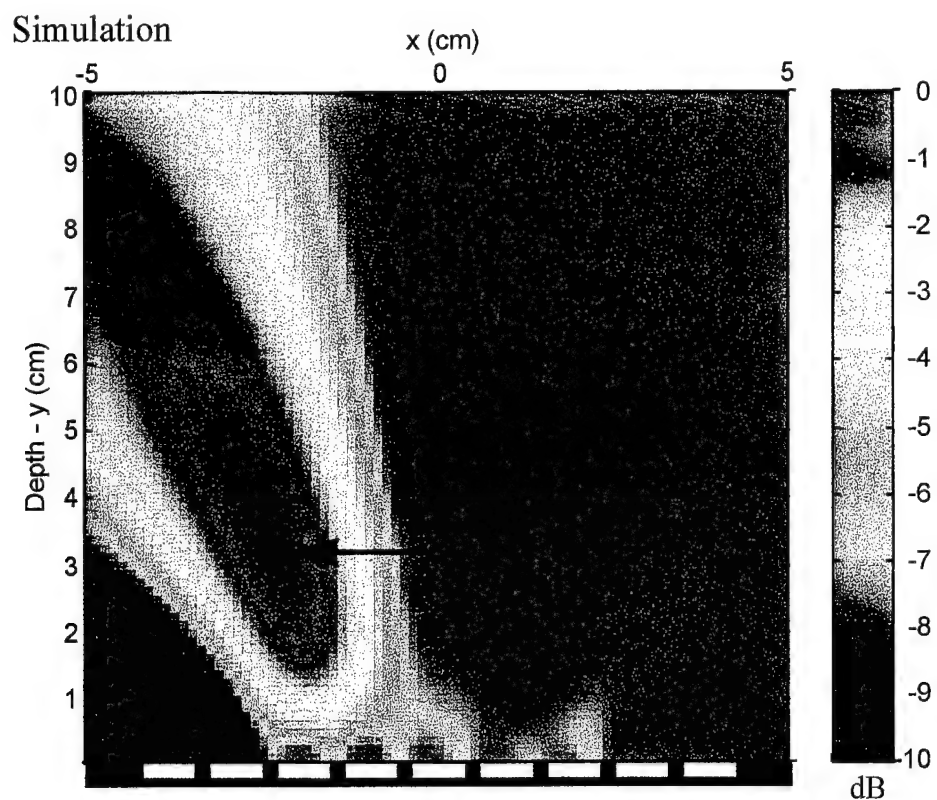


Figure 16. Simulation and Experimental Data of CFB for Experiment Two at 200 Hz

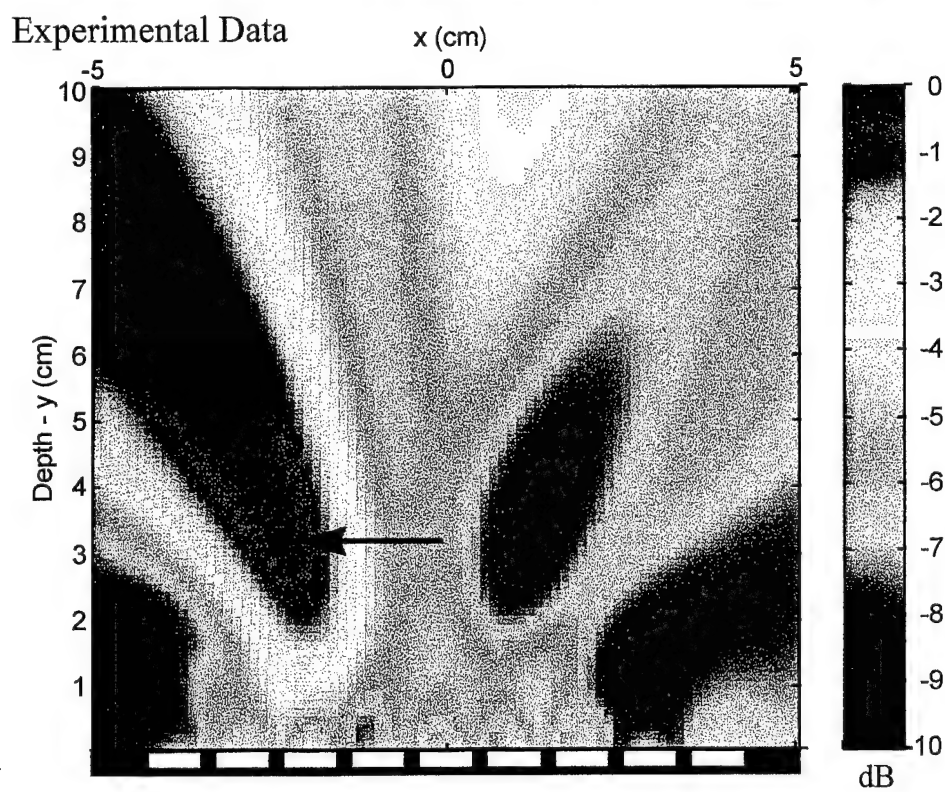
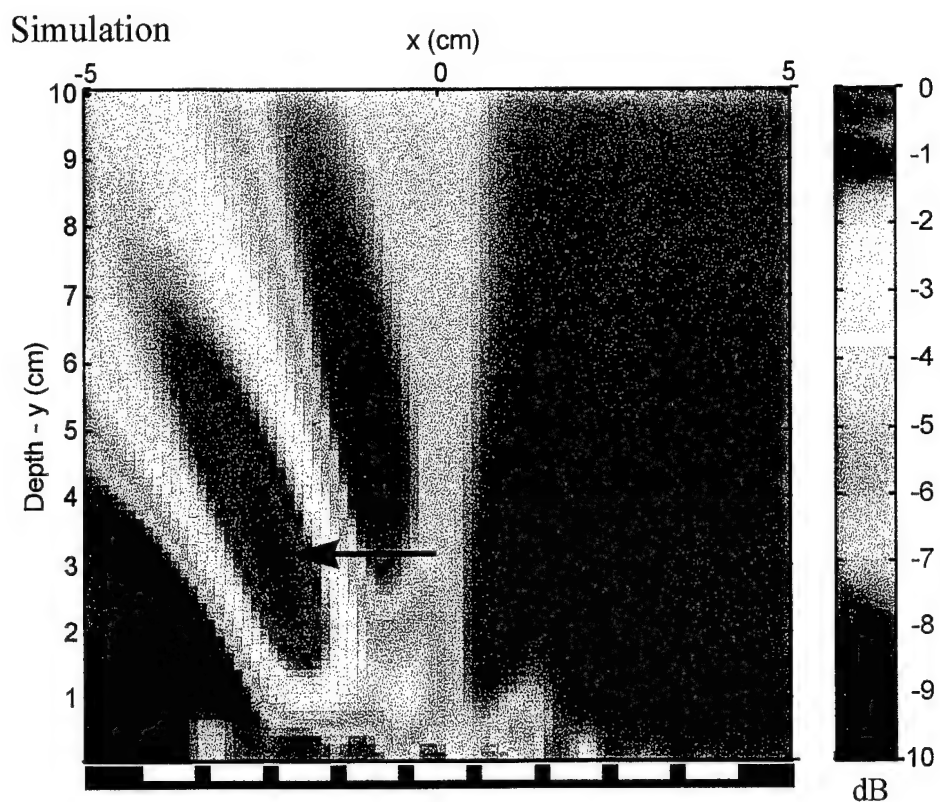


Figure 17. Simulation and Experimental Data of CFB for Experiment Two at 300 Hz

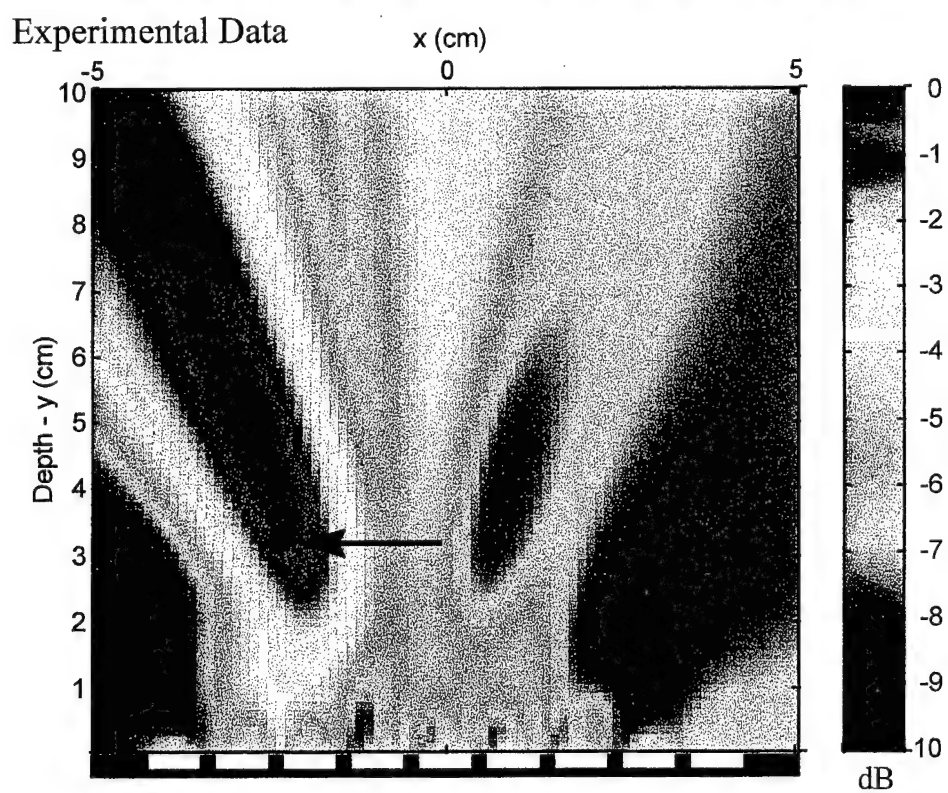
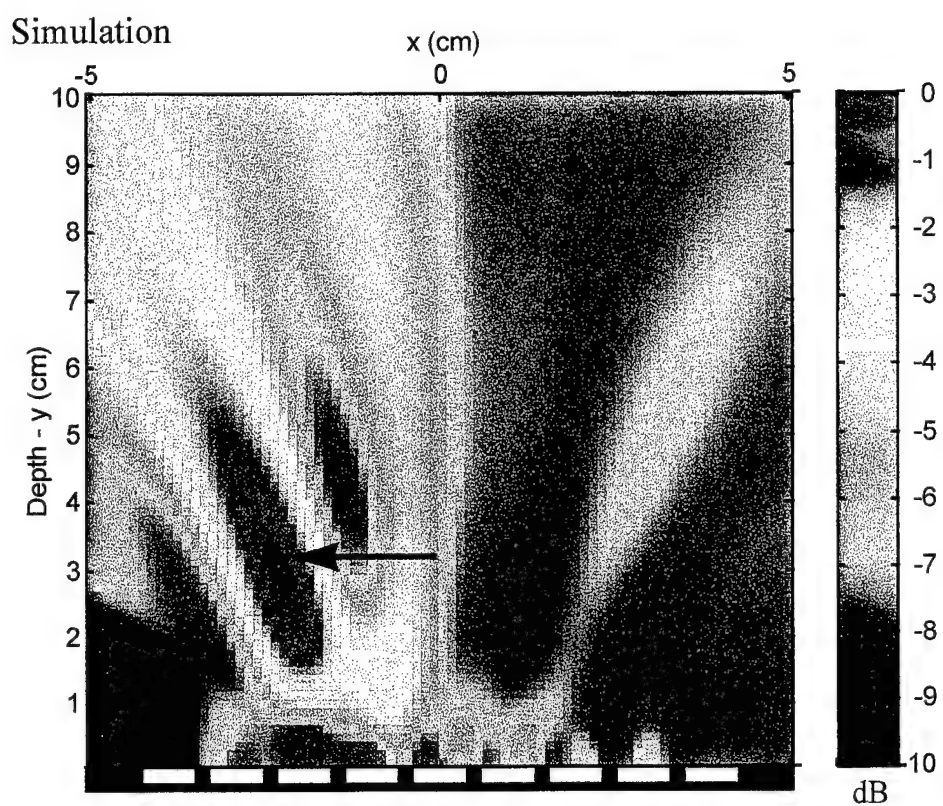


Figure 18. Simulation and Experimental Data of CFB for Experiment Two at 400 Hz

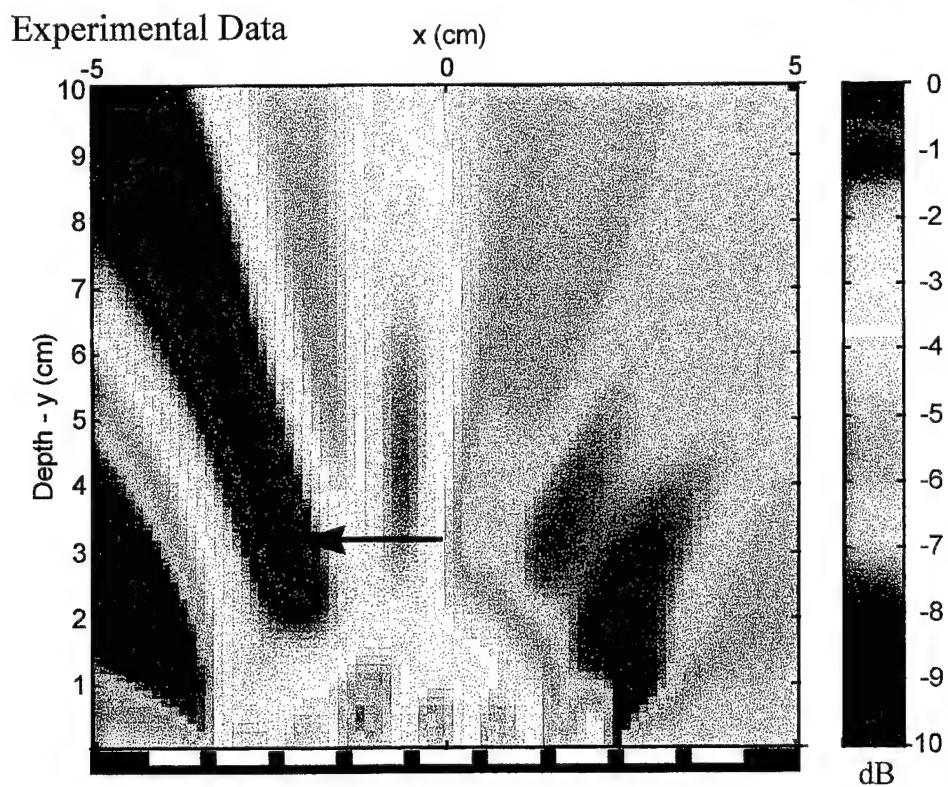
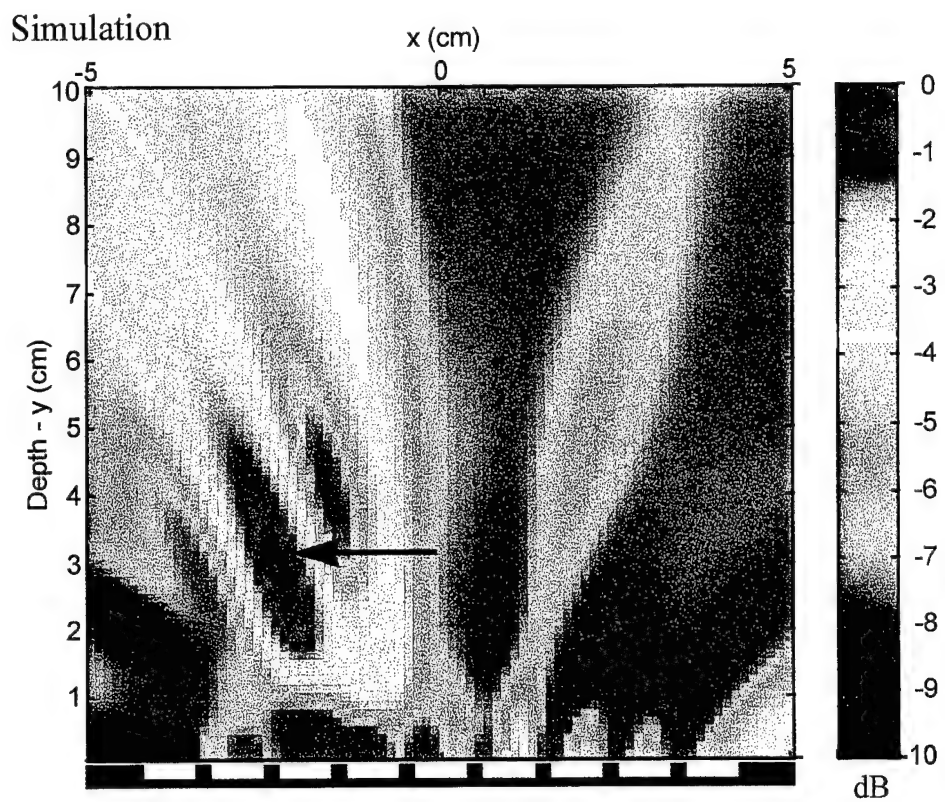


Figure 19. Simulation and Experimental Data of CFB for Experiment Two at 500 Hz

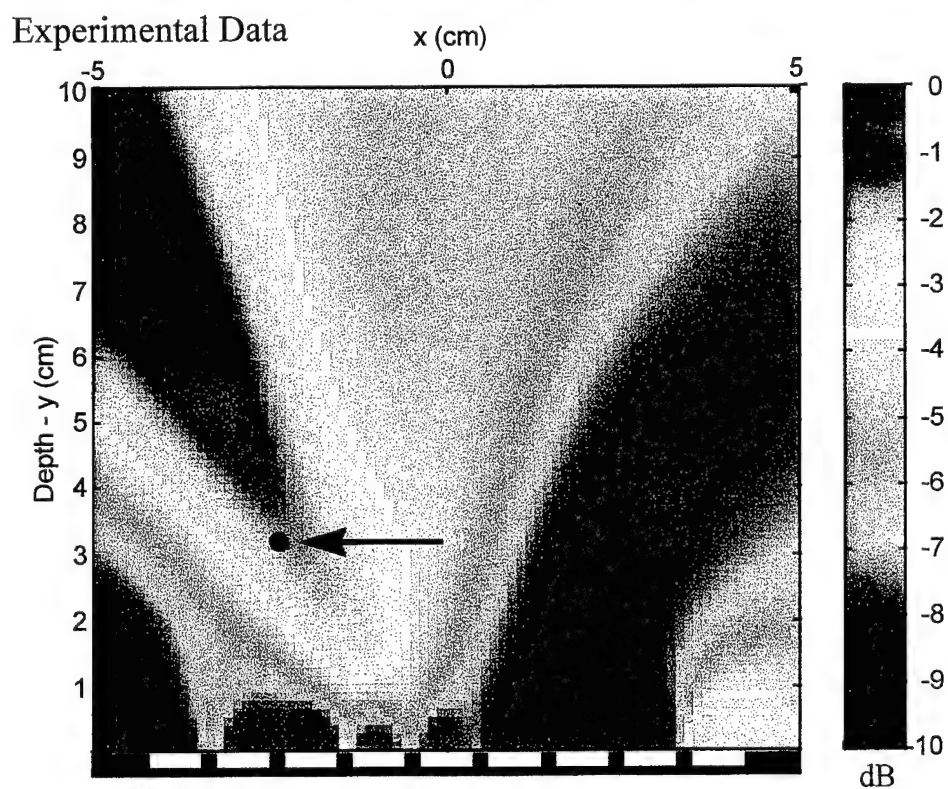
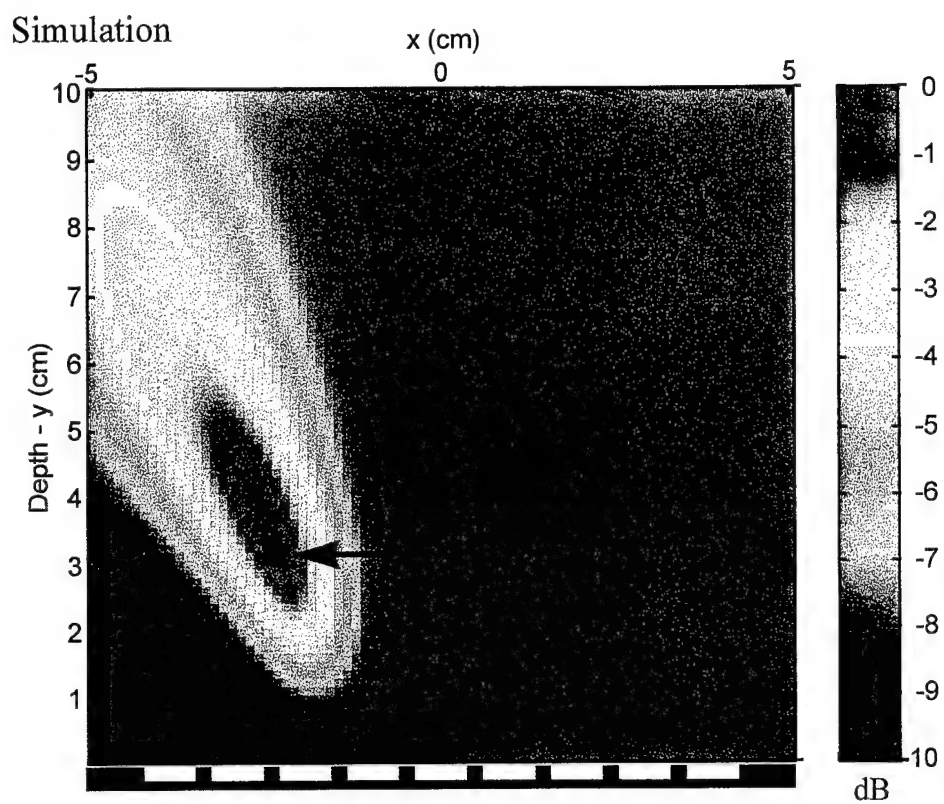


Figure 20. Simulation and Experimental Data of RVDR Focused Beamformer for Experiment Two at 200 Hz

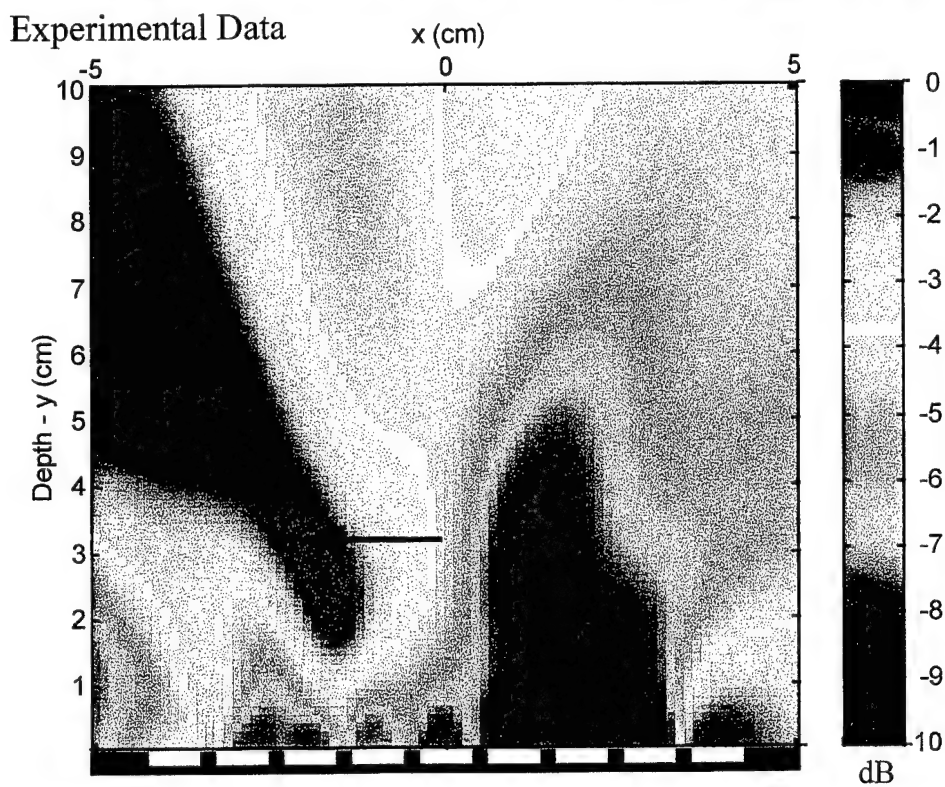
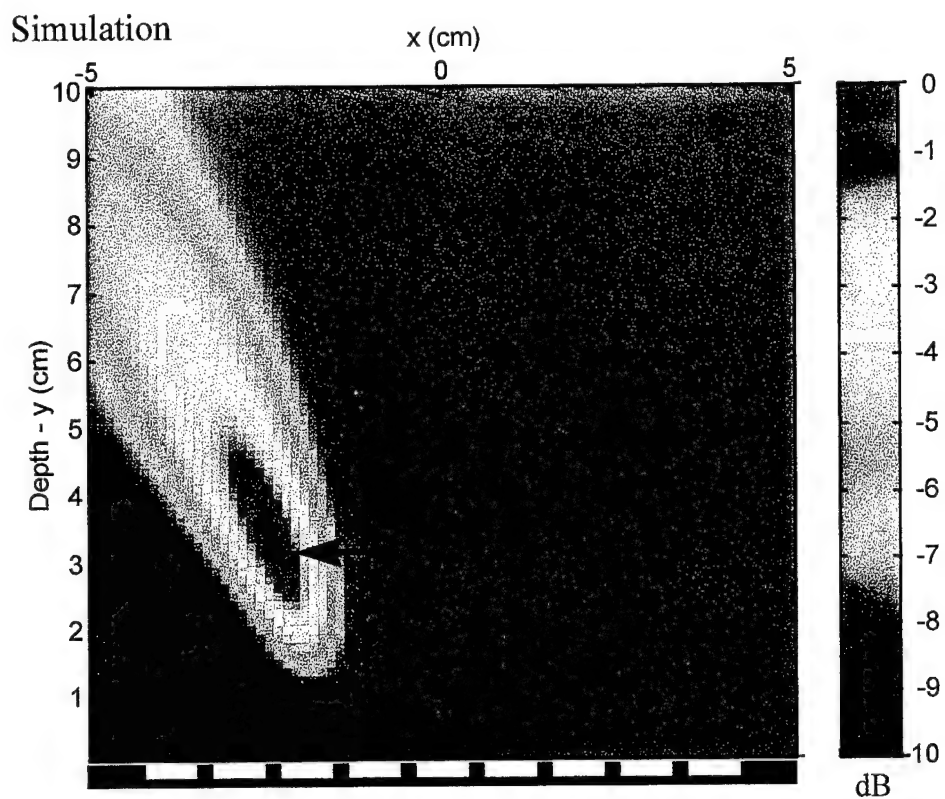


Figure 21. Simulation and Experimental Data of RVDR Focused Beamformer for Experiment Two at 300 Hz

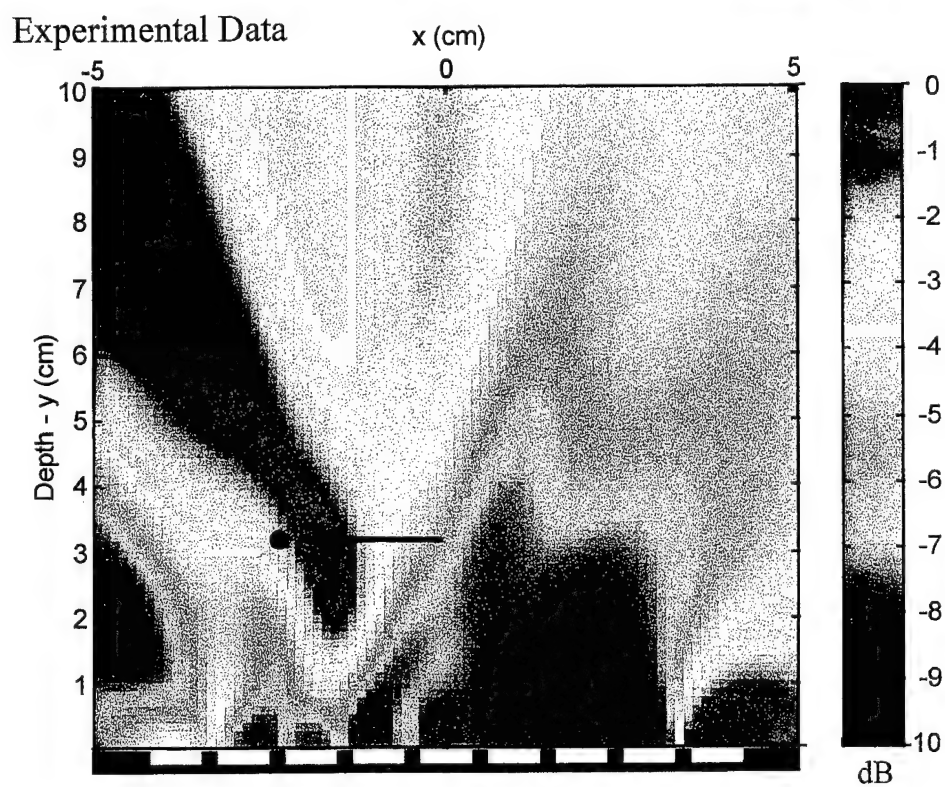
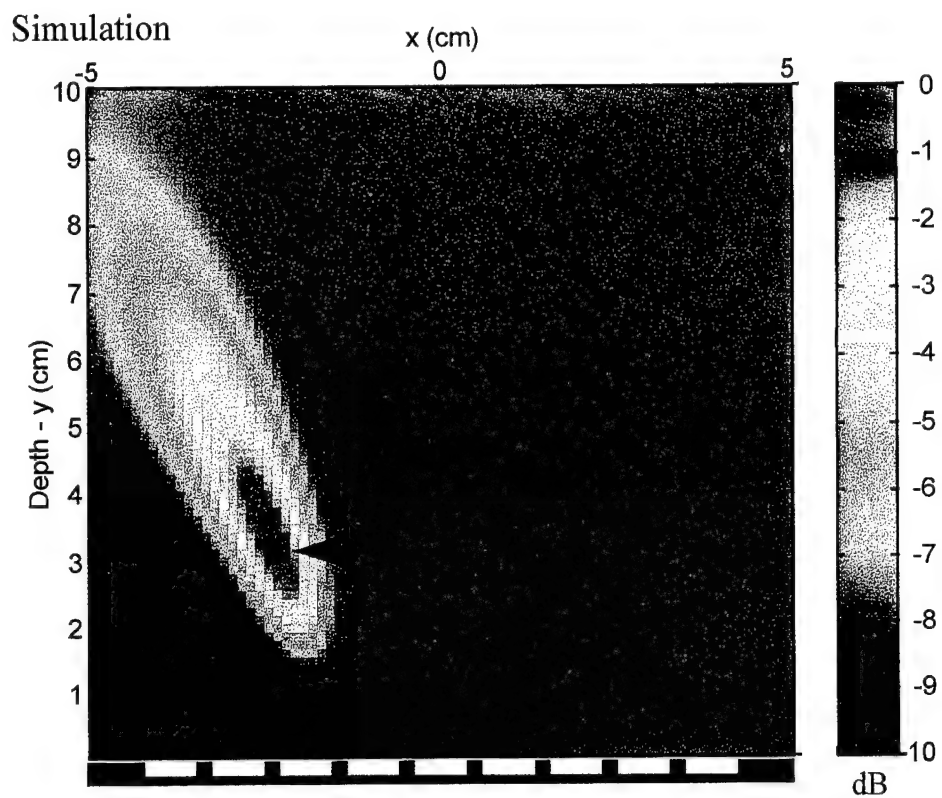


Figure 22. Simulation and Experimental Data of RVDR Focused Beamformer for Experiment Two at 400 Hz

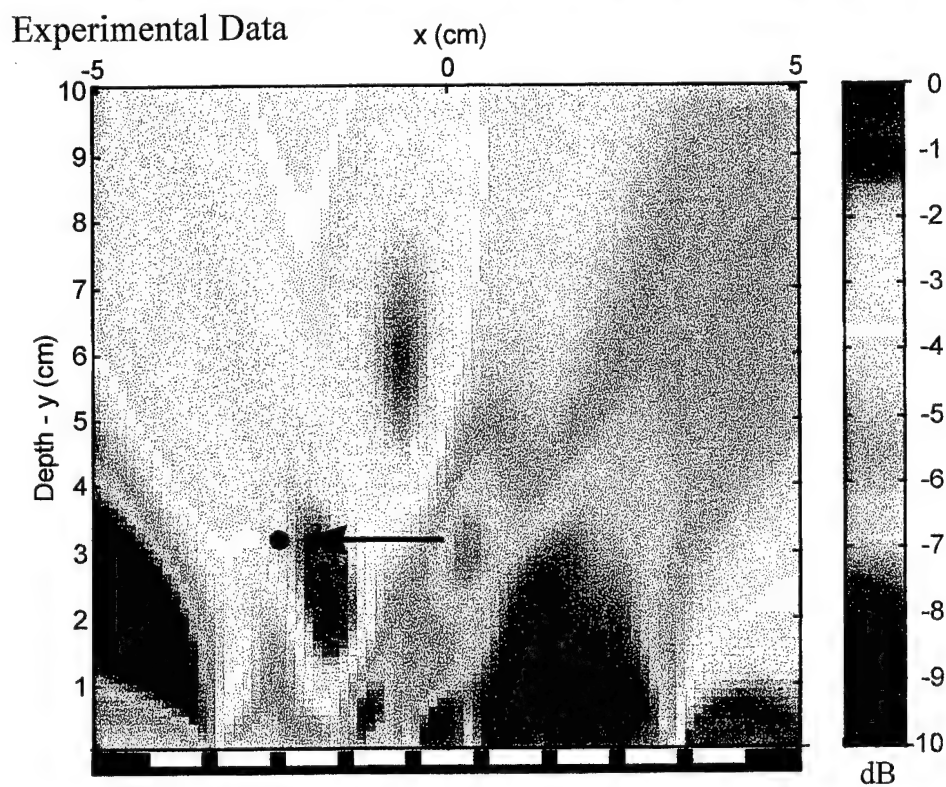
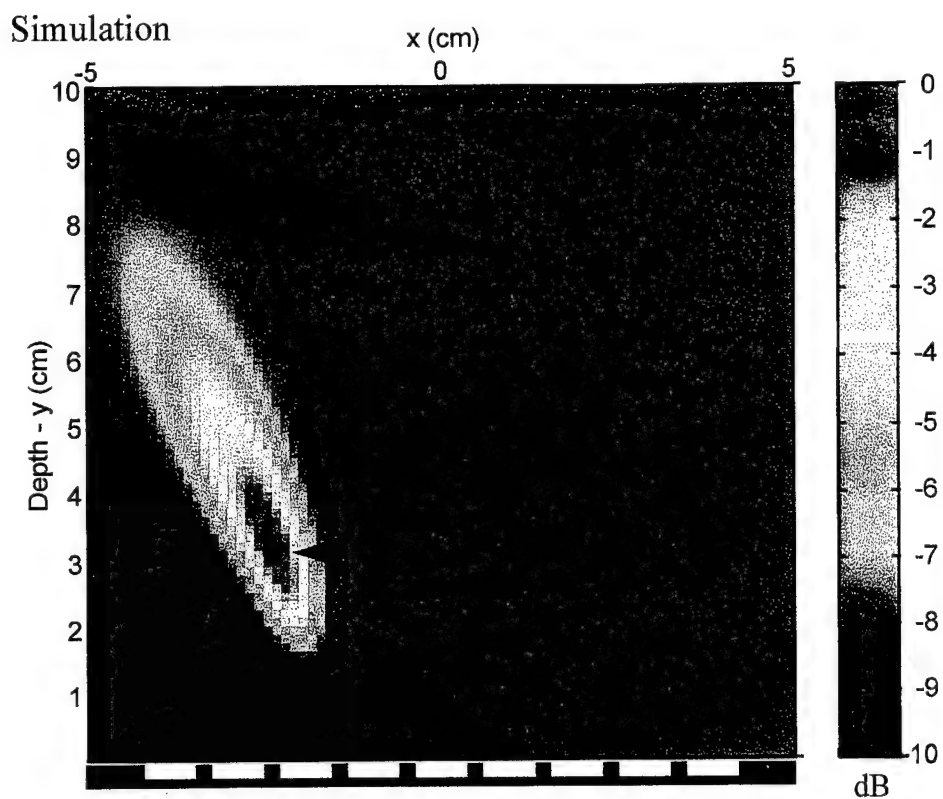


Figure 23. Simulation and Experimental Data of RVDR Focused Beamformer for Experiment Two at 500 Hz

The CFB and the RVDR focused beamformers each produced images that accurately detected and localized the blockage. The CFB-measured images were slightly better than the RVDR-measured images, especially in the second experiment. This is typically the result of a model parameter mismatch between beamformer parameters and actual measurement values. High-resolution beamformers (such as the RVDR beamformer) tend to be substantially more sensitive to parametric mismatch than conventional beamformers. Specifically, errors in shear wave speed, sensor position, spatial coherence of the noise, spatial coherence of the source, and geometric spreading loss factor will produce model mismatch that distorts the beamformed image to varying degrees.

The images have better resolution as the frequency increases. This is a result of the shorter wavelength energy producing a beam with a smaller area. In addition, beams that are produced with this type of imaging algorithm provide less resolution as the distance of the focal point into the imaged volume increases. The image depth of 3.18 cm (1.25 in.) was chosen because this is the shortest distance from the chest wall to the left anterior descending coronary artery in the average human.¹⁴

It is noted that the simulations and experimental data are in good, although not exact, agreement. There are several possible reasons for this variance:

- The turbulent energy is modeled with a line segment source that has no physical extent in the radial direction, whereas the experiment uses a tube that is 1/8 inch in diameter.
- The point-to-point correlation function of the source model was derived from a flat plate model, whereas the point-to-point correlation of the tube may be slightly different.
- The line segment source model used was an rms pressure frequency-independent measurement rather than a frequency-dependent measurement that could have a different spatial shape at each frequency.

Additionally, the blockage used in the previous source measurements³ had a blunt inlet region compared with the tapered inlet region used in this experiment. Nevertheless, the sidelobe energy in most of the measurement images is in approximately the same locations as the corresponding numerical simulations, which is a good indication that the source model in the

simulations is similar to the actual turbulent energy in the experiment. Finally, the background noise assumed in the numerical simulations is spatially uncorrelated with zero mean and uniform variance, whereas the noise in the actual experiment could have angular extent. This type of noise mismatch in the model would cause a bias error for energy location because the focusing process has inaccurately described the effective noise spatial extent.

6. CONCLUSIONS AND RECOMMENDATIONS

In summary, the turbulent flow energy in and downstream from the occlusion creates a normal wall pressure on the tube that is converted to (predominantly) shear waves in the solid at frequencies of 100 to 500 Hz. These waves propagate to the surface where they can be measured by an array signal processing system that includes nearfield beamforming algorithms to perform imaging of the spatial shear wave field. Imaging the volumetric region under the array produces an accurate representation of the internal energy field. The use of a -3 dB contour image deflection criterion in the study allows the occlusion to be detected and localized to within 1 cm of depth and crossdepth.

Further research should investigate the capability of this method to more accurately locate the blockage and more fully characterize the temporal spectrum of energy that it produces. Moreover, it is recommended that embedded stiffeners representing the rib cage be added to the urethane mold. This will change the energy sensed by the array because the waves will scatter off and reradiate from high-density objects in the solid. Such volumetric inhomogeneity will be far more representative of the *in vivo* conditions that the experiment must replicate to achieve the ultimate goal of this effort, which is the detection of early stage arterial disease in the human body.

7. REFERENCES

1. N. L. Owsley, A. J. Hull, M. H. Ahmed, and J. Kassal, "A Proof-of-Concept Experiment for the Detection of Occluded Coronary Arteries Using Array Sensor Technology," *1995 IEEE Engineering in Medicine & Biology 17th Annual Conference*, Montreal, Canada, September 1995.
2. A. J. Hull and B. M. Abraham, "Space-Time Analysis of the Flow-Induced Vibration of a Solid Containing an Embedded Cylindrical Shell," NUWC-NPT Technical Report 11,073, Naval Undersea Warfare Center Division, Newport, RI, 1995.
3. R. J. Tobin and I. Chang, "Wall Pressure Spectra Scaling Downstream of Stenosis in Steady Tube Flow," *Journal of Biomechanics*, vol. 9, 1976, pp. 633-640.
4. S. Haykin, J. N. Justice, N. L. Owsley, J. L. Yen, and A. C. Kak, *Array Signal Processing*, Prentice-Hall, Inc., Englewood Cliffs, New Jersey, 1985.
5. W. L. Keith and B. M. Abraham, "Effects of Convection and Decay of Turbulence on the Wall Pressure Wavenumber-Frequency Spectrum," *Journal of Fluids Engineering*, vol. 119, 1997, pp. 50-55.
6. J. Verburg, "Transmission of Vibrations of the Heart to the Chestwall," *Advanced Cardiovascular Physiology*, Karger, Basel, vol. 5 (part III), 1983, pp. 84-103.
7. S. A. Jones and A. Fronek, "Analysis of Break Frequencies Downstream of a Constriction in a Cylindrical Tube," *Journal of Biomechanics*, vol. 20, no. 3, 1987, pp. 319-327.
8. S. A. Ahmed and D. P. Giddens, "Velocity Measurements in Steady Flow Through Axisymmetric Stenosis at Moderate Reynolds Numbers," *Journal of Biomechanics*, vol. 16, no. 7, 1983, pp. 505-516.
9. S. A. Ahmed and D. P. Giddens, "Flow Disturbance Measurements Through a Constricted Tube at Moderate Reynolds Numbers," *Journal of Biomechanics*, vol. 16, no. 12, 1983, pp. 955-963.
10. C. Clark, "Turbulent Velocity Measurements in a Model of Aortic Stenosis," *Journal of Biomechanics*, vol. 9, 1976, pp. 677-687.

11. C. Clark, "Turbulent Wall Pressure Measurements in a Model of Aortic Stenosis," *Journal of Biomechanics*, vol. 10, 1977, pp. 461-472.
12. W. H. Pitts and C. F. Dewey, "Spectral and Temporal Characteristics of Post-Stenotic Turbulent Wall Pressure Fluctuations," *Journal of Biomechanical Engineering*, vol. 101, May 1979, pp. 89-95.
13. R. W. Fox and A. T. McDonald, *Introduction to Fluid Mechanics*, John Wiley & Sons, Inc., New York, 1973.
14. C. A. Norton, "A Compilation of Geometric Distance and Tissue Property Data for the Human Thorax," NUWC-NPT Technical Document 11,037, Naval Undersea Warfare Center Division, Newport, RI, 1995.

INITIAL DISTRIBUTION LIST

Addressee	No. of Copies
Office of Naval Research (ONR 321: T. G. Goldsberry, K. Dial, R. Varley)	3
Defense Technical Information Center	12
Analysis and Technology, Inc. (J. Kassal)	1
MedAcoustics Corp. (A. Eberhardt (3), C. Chassaing (3))	6
Massachusetts General Hospital (R. Levine, MD)	2